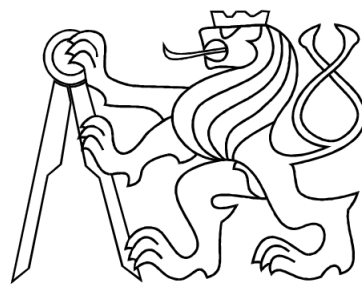


CZECH TECHNICAL UNIVERSITY IN PRAGUE
FACULTY OF NUCLEAR SCIENCES AND
PHYSICAL ENGINEERING
DEPARTMENT OF PHYSICS



Bachelor Thesis

Magnetic field configurations and their
measurement on tokamak GOLEM

Author: Tomáš Markovič

Supervisor: Ing. Ivan Ďuran, Ph.D.

Prague, 2010

Prohlášení

Prohlašuji, že jsem svou diplomovou práci vypracoval samostatně a použil jsem pouze podklady (literaturu, projekty, SW atd.) uvedené v příloženém seznamu.

Nemám závažný důvod proti užití tohoto školního díla ve smyslu § 60 Zákona č.121/2000 Sb. , o právu autorském, o právech souvisejících s právem autorským a o změně některých zákonů (autorský zákon).

V Praze dne _____

_____ podpis

Acknowledgements

First of all I would like to thank to Ing. Ivan Ďuran, Ph.D. for his supervision, numerous valuable suggestions and advices and for his patient guidance on the field of research over the course of past two years. Furthermore, I am thankful to Ing. Vojtěch Svoboda, Csc. for his time spent supervising numerous experiments on tokamak, even though they sometimes lasted long in the night. Finally I would like to express my endless gratitude to my family, as without their support and understanding this work probably could not come into existence.

Název práce: Konfigurace magnetických polí a jejich měření na tokamaku GOLEM

Autor: Tomáš Markovič

Obor: Fyzikální inženýrství

Druh práce: Bakalářská práce

Vedoucí práce: Ing. Ivan Ďuran, Ph.D., Ústav fyziky plazmatu, AV ČR

Abstrakt:

V práci je uveden základní přehled konfigurací magnetického pole v tokamaku, včetně způsobů jeho měření. Nakolik nejběžněji používané magnetické senzory jsou induktivní povahy, je podána diskuse o výhodách a nevýhodách dvou hlavních konceptů analogové integrace. Jelikož je v posledním čase galvanometrickým sensorům založeným na Hallově efektu věnována zvýšená pozornost, nakolik nepotřebují integraci, také jim je věnován prostor. Společně s popisem konfigurace magnetického pole na tokamaku GOLEM je v práci také obsažena diskuse o nynějším stavu jeho magnetické diagnostiky s návrhy na její zlepšení. Na dvou odlišných experimentech je demonstrován rozsah spolehlivosti Mirnovových cívek používaných k měření lokálního magnetického pole. V prvním experimentu dává modelování poloidálního magnetického pole náhled do permeability komory. Druhý experiment je věnován první aproximaci plazmového prstence s použitím sensorů lokálního magnetického pole. Také je uvedena metoda eliminace parazitního signálu toroidálního magnetického pole v signálech sensorů poloidálního pole.

Klíčová slova: Tokamak GOLEM, Hallovy sondy, Mirnovovy cívky, magnetická diagnostika, analogová integrace, modelování poloidálního pole, odhad polohy plazmatu.

Title: Magnetic field configurations and their measurement on tokamak GOLEM

Author: Tomáš Markovič

Abstract:

Basic overview of configurations of magnetic field in a tokamak, along with means of its measurement is provided. Since most common magnetic diagnostics sensors presently used are of inductive nature, pros and cons of two main concepts of analog integration are discussed. As galvanometric sensors such as Hall probes have been getting more attention lately as they do not require integration, characterization of these sensors is included. Along with description of magnetic field configurations on tokamak GOLEM, discussion concerning present state of its magnetic diagnostics with proposals of its modification is included as well. Extension of reliability range of Mirnov coils used for local magnetic field measurements is demonstrated on two different experiments. In the first experiment, modeling of poloidal magnetic field gives insight into permeability of chamber. The other experiment is aimed on first approximation of plasma column position with simple use of local magnetic field sensors. Additionally, a method of toroidal magnetic field cross-talk elimination in signal of poloidal magnetic field sensors is described.

Key Words: Tokamak GOLEM, Hall probes, Mirnov coils, magnetic diagnostics, analogue integration, poloidal field modeling, plasma position estimation.

Contents

List of Figures	vii
List of Tables	xi
1 Introduction	1
2 Fusion, Plasma and its Confinement	3
2.1 Fusion Reactions	3
2.2 Plasma State of Matter	5
2.3 Lawson Criterion	5
2.4 Confinement	6
3 Magnetic Field in Tokamak and its Diagnostics	9
3.1 Tokamak Concept	9
3.2 Particle Drifts and Magnetic Field Configuration	11
3.3 Magnetic Diagnostics	14
3.3.1 Rogowski Coil	14
3.3.2 Magnetic Coil	15
3.3.3 Poloidal Flux Loop	18
3.3.4 Hall Probes	18
4 Tokamak GOLEM	21
4.1 Overall Characteristics	21
4.2 Configuration of Electric and Magnetic Fields	25
4.2.1 System of Toroidal Electric Field Generation	25
4.2.2 System of Toroidal Magnetic Field Generation	26
4.2.3 System of Stabilization Magnetic Field Generation	26
4.3 Magnetic Diagnostics	26

4.3.1	Rogowski Coils	27
4.3.2	Flux Loops	28
4.3.3	Mirnov Coils	29
4.3.4	Saddle Coil	31
4.3.5	Toroidal Magnetic Field Measurement Coils	31
4.3.6	Hall Probes	32
5	Modeling and Measurement of Poloidal Magnetic Field	35
5.1	Numerical Evaluation of Magnetic Field Induction by Use of Biot-Savart's Law	35
5.2	Arrangement of B Measurement with Hall Probes	37
5.3	Arrangement of B Measurement with Mirnov Coils	40
5.4	Results and Analysis of the Measurements	41
6	Plasma Position Estimation	47
6.1	Theory of Plasma Position Determination and Used Approximation	47
6.2	Subtraction of Toroidal Magnetic Field Cross-Talk	50
6.3	Results and Analysis	51
7	Summary	57
	References	59

List of Figures

3.1	Scheme of the tokamak. The figure was obtained from [7].	9
3.2	Scheme of particle drifts in tokamak. \mathbf{B} stands for toroidal magnetic field, \mathbf{E} for electric field induced by separation of charges due to drift from equation 3.8, hence \mathbf{v} represents drift from equation 3.9. ι denotes rotational transport from equation 3.10.	13
3.3	Scheme of Rogowski coil from literature [3]. Area A is equivalent to S from equation 3.13.	15
3.4	Scheme of passive (above) and active (below) integrating circuit from literature [16]. R stands for resistivity, C for capacity and G denotes gain of operational amplifier.	17
3.5	Figure from literature [11] of Hall plate. $C1$ and $C2$ are contacts for implementation of external current I , while $S1$ and $S2$ are contacts for measurement of induced Hall voltage V_H . Dimensions of the plate are characterized by w , l and t . Outer magnetic field induction is represented by B	19
4.1	Present status of tokamak GOLEM. Tokamak itself is on the left panel while room for containment of energizing systems is on the right panel.	21
4.2	A sample from liner replaced in 1984, encircled by coil of toroidal magnetic field generation.	22
4.3	An engineering scheme of the tokamak GOLEM, obtained from [18].	23
4.4	An example of typical evolution of basic measured parameters. U_{loop} stands for loop voltage, B_t represents toroidal magnetic field, I_p is current of plasma and $PhotoD$ is signal from photodiode measuring radiation from chamber on wavelengths of visible light. In the case of interest, analysis of this shot can be found in [18].	24
4.5	Coils of toroidal electric field generation.	25

4.6	Coils of toroidal and poloidal magnetic field generation.	25
4.7	Scheme of compensation windings with corresponding polarities of currents. B_H stands for coils of horizontal stabilization field generation, B_V denotes coils of vertical field and B_V^{in} represents coils of vertical field, placed under the coating. Scheme can be found in literature [3], while configuration of currents is described in [1].	27
4.8	Scheme of present magnetic diagnostics of tokamak Golem with their respective data acquisition systems. <i>Rog</i> stands for Rogowski coil described in section 4.3.1, <i>Flux Loop</i> is described in section 4.3.2, <i>Tor.Coil</i> stands for sensor from section 4.3.5 and <i>Saddle Coil</i> is described in section 4.3.4. Finally, <i>Mirnov Coils</i> are described in section 4.3.3. <i>DAS 1</i> and <i>DAS 2</i> denote data acquisition systems described in section 4.1.	28
4.9	Figure of large Rogowski coil encircling vacuum vessel of tokamak and both of the flux loops together.	29
4.10	Small Rogowski coil used for measurement of currents flowing through conductors.	29
4.11	Small coil used for toroidal magnetic field measurement.	32
4.12	A diagnostic ring with Hall probes. Image was obtained from [5].	33
4.13	Allegro A1322LUA type chip with integrated Hall transducer in the center. Image can be found in [14].	33
5.1	Scheme for purposes of algorithm explanation. Location of sensor (e.g. place where \mathbf{B} is being calculated) is represented by vector with full line and corresponds to coordinates $[y_s; z_s]$. Coil generating \mathbf{B} is in given poloidal plane represented by dashed vector with coordinates $[y_0; z_0]$. Element of coil, whose contribution to \mathbf{B} is calculated, is connected with center of coordinate system by a full line vector. Relative distance between the sensor and this element (of length dl) is represented by full line vector denoted \mathbf{R} . φ stands for toroidal angle. Please note that axis x is inverted.	36
5.2	Scheme of circuit used for energizing of poloidal coils. C denotes capacitor described in section 5.2.	38
5.3	Locations of used Hall probes on the diagnostic ring.	39
5.4	An example of current discharges driven through poloidal coils during experimental arrangement with Hall probes (panel on the left) and experimental arrangement with Mirnov coils (panel on the right).	40

5.5	Measurement of vertical magnetic field \mathbf{B} on low-field side of liner. Measurement with Hall probe is on the left panel, while measurement with Mirnov coil is on the right panel.	42
5.6	Measurement of vertical magnetic field \mathbf{B} on high-field side of liner. Measurement with Hall probe is on the left panel, while measurement with Mirnov coil is on the right panel.	43
5.7	Measurement of vertical magnetic field \mathbf{B} on the top of liner, made with a Hall probe.	43
5.8	Measurement of horizontal magnetic field \mathbf{B} on the top of liner. Measurement with Hall probe is on the left panel, while measurement with Mirnov coil is on the right panel.	44
5.9	Measurement of horizontal magnetic field \mathbf{B} on low-field side of liner, made with a Hall probe.	44
5.10	Measurement of horizontal magnetic field \mathbf{B} on high-field side of liner, made with a Hall probe.	45
5.11	Measurement of horizontal magnetic field \mathbf{B} on the bottom of liner, made with a Mirnov coil.	45
6.1	Position shift of plasma column (depicted as circle inside of liner) towards low-field side. Dashed circle represents limiter. b denotes distance from center of liner to Mirnov coils and Δ_{LFS} is shift itself. $MC01 - MC13$ denote Mirnov coils, where $MC01$ measures magnitude of magnetic field induction B_1 , $MC05$ measures B_5 , $MC09$ measures B_9 and $MC13$ measures B_{13}	49
6.2	An example of Mirnov coil data. The elimination of toroidal magnetic field cross-talk is described in section 6.2.	52
6.3	Current and flux voltage evolution of shot 2792.	53
6.4	Evolution of average toroidal magnetic field during shot 2792, evaluated by method described in section 4.3.5.	54
6.5	Graph on the left panel shows displacement of plasma column towards low-field side, calculated by equation 6.9. Graph on the right panel shows displacement of plasma column towards top, calculated by equation 6.10. Data are relevant for shot 2792.	55
6.6	Current and flux voltage evolution of shot 2794.	55

6.7	Evolution of average toroidal magnetic field during shot 2794, evaluated by method described in section 4.3.5.	56
6.8	Graph on the left panel shows displacement of plasma column towards low-field side, calculated by equation 6.9. Graph on the right panel shows displacement of plasma column towards top, calculated by equation 6.10. Data are relevant for shot 2794.	56

List of Tables

4.1	Characterization of large Rogowski coil. l denotes overall length of the coil, D_{wire} is the diameter of wire of the coil and D_{inner} the diameter of the coil itself. n represents number of turns of the coil per unit length and K_1 stands for calibration constant.	30
4.2	Characterization of Mirnov coils. L denotes inductance, R stands for resistance, D_{wire} denotes the diameter of the wire of the coil, N stands for total number of turns in each coil. There are two layers of turns with diameters D_{inner} and D_{outer} respectively.	30
4.3	Properties of integrated circuits of Hall probes. T_{oper} stands for interval of operating temperature, f is maximal frequency of the signal. K_{sens} stands for nominal sensitivity of the single integrated sensor. V denotes supply voltage of each sensor.	34
5.1	Calibration constants for Hall probes. The set-up of the probes on the SK ring can be found in fig. 5.3.	38
6.1	K_C constants for elimination of toroidal magnetic field cross-talk on Mirnov coils (see equation 6.15). Configuration of Mirnov coils is in fig. 6.1. No value in the case of $MC13$ means that misalignment of this coil was not detected.	51

Chapter 1

Introduction

In the whole history of mankind, the main source of conflicts among people has undoubtedly been their different opinions on correct distribution of natural resources. When industrial revolution took place, people started to have increased interest in a new type of natural resources - the energy resources. First energy resources ever used were fossil fuels, known from prehistoric times and massively used in 19. century. However, their distribution in Earth crust is highly inhomogeneous, being especially evident in the case of raw oil. Even though the fossil fuels cover most of present world energy consumption, because of their eventual depletion it will not be possible to continue in this trend for an indefinite long time. It is unlikely that the world energy consumption would massively decrease in the near future, for current trends show the opposite. Since for its sustainable development will mankind need even more energy than today, it is necessary not only to seek new energy resource deposits, but to develop new means of obtaining energy as well. One of the most promising methods is the use of energy released by the fusion of nuclei. As it will be explained later, the main advantages of fusion energy are high availability of fuel, virtually no risk of pollution and no danger of fuel deposits depletion. Possibility of large-scale energy production, necessary for existence of larger agglomerations, makes fusion energy even more attractive. Although it is unlikely that current types of power-plants would be massively replaced, fusion energy still has potential to become vital part in economy of energetic mix in mid-near future.

Chapter 2

Fusion, Plasma and its Confinement

2.1 Fusion Reactions

There are two possible approaches how to obtain energy from the atomic nuclei. First of them is fission of heavy nuclei. As the heavier nucleus decays into more stable nuclei with higher binding energy per nucleus, the difference in overall binding energy before and after the reaction is released in form of kinetic energy of products. However, only by fission of elements heavier than ${}^{56}\text{Fe}$ (the most stable isotope with highest value of binding energy per nucleon), a positive amount of energy can be obtained. The other approach is to fuse light nuclei into heavier elements, more stable than the reactants. In this process, enormous amount of energy is released (again in the form of kinetic energy of reaction products). Both fission and fusion reactions are based on strong force interaction in the nucleus. Although on Earth fusion of nuclei rarely occur in other cases than in specially designed experiments, in the Universe as a whole is this process much more common than fission, being a source of energy in stars.

The core of stars is initially a proton gas with traces of helium. According to [6], the primary reaction initiating fusion cycle is reaction of two protons:

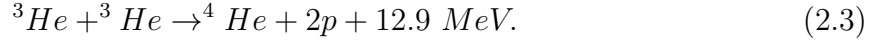


Here D stands for deuterium (${}^2\text{H}$ isotope) and μ represents neutrino. Although this reaction is based on weak interaction (hence the μ) and thus is not a pure fusion reaction, it is essential for generation of deuterium, which serves as fusion fuel in next reaction:



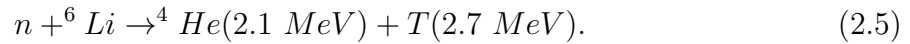
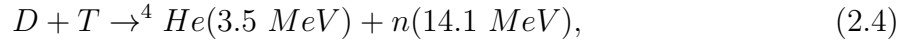
In Sun-like stars, resulting ${}^3\text{He}$ nucleus mostly fuses with another ${}^3\text{He}$ to form an α

particle, while two protons are released:



This cycle is the main energy source of these stars, however, also other cycles are present (especially in more massive stars), where heavier nuclei are produced.

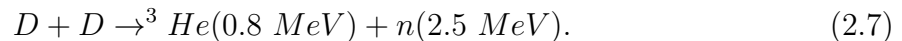
For industrial purposes however, a different set of fusion reactions will have to be used. This is mainly because conditions inside core of a star are very different from conditions in a potential fusion reactor. As mentioned in [2], the first generation of fusion reactors will undoubtedly use following reactions:



In expressions above, T denotes tritium, equal to ${}^3\text{H}$ isotope of hydrogen. The main reaction of the fuel cycle is described by equation 2.4. In this reaction, one of the products is a high-energy neutron, carrying roughly 4/5 of the reaction overall energy, which will be used in the energetic cycle of the future power-plant. This neutron is also used in reaction described by equation 2.5 to further support the main fuel cycle by producing tritium fuel from lithium blanket. Even though these high-energy neutrons will enable more homogeneous distribution of energy in reactor wall, an unprecedented damage to the wall will be caused in the process. This difficulty could be overcome by using different reaction as a main fuel cycle [2]:



or the other variation, occurring with almost the same probability:



However, conditions of these reactions are more difficult to reach than conditions of reaction 2.4. Additionally, even though neutrons from these reactions have significantly lower energies, one of products in reaction 2.6 is tritium. Since conditions for reaction 2.4 to occur are not as strict as the ones for reaction 2.6 or 2.7, tritium produced from reaction 2.6 will fuse with deuterium fuel according to equation 2.4. Resultantly, high-energy neutrons (although less numerous) will be produced again. According to [2] and [6], there are even more possible fusion reactions which could be economically viable in

the future. One of the main advantages of mentioned fusion reactions is, that all the reactants in reactions 2.4 - 2.7, except for tritium, are highly abundant and available in the nature. Additionally, tritium for the first generation of reactors can be bred inside reactor vessel by reaction 2.5. The required lithium can be extracted from lithium ore, which is abundant in Earth's crust.

2.2 Plasma State of Matter

As was mentioned before, fusion reactions are based on strong interaction. However, effective range of this interaction is $\sim 10^{-15}$ m. For two protons, this barrier is equivalent to energy of 0.4 MeV (see literature [6]). Fortunately, it is not necessary for fusion fuel to reach such a high temperatures thanks to the quantum tunneling effect. For conversion between energy and temperature, relation in form of $1 \text{ eV} = 1.1604 \cdot 10^4 \text{ K}$ is assumed (accordingly to [8]). Despite that, resultant energy barrier is still hard to overcome (at least technologically on larger scales). However, should the fusion fuel had Maxwell distribution, the particles of energetic tail would have enough energy to enter fusion reaction (according to [2]). Thermal condition for such a medium, using reaction 2.4, would be $\sim 10^8 \text{ K}$. This temperature is much lower as in other reactions mentioned above, thanks to ability of reactants to form resonance nucleus of ${}^5\text{He}$. Taking into consideration that ionization potential of hydrogen is 13.6 eV (according to [6]), it is evident that in thermal fusion experiments (e.g. the ones working with Maxwellian distributed medium), the work gas is completely ionized. Such a state of matter is called plasma. Many properties of plasma are summarized in its definition (stated in literature [2]): *Plasma is quasi-neutral gas of ionized and neutral particles which exhibits collective behavior*. Ionization and collective behavior of fusion medium affect construction designs of fusion reactors concepts into large extent, as it will be explained in chapter 3.

2.3 Lawson Criterion

It was mentioned before that as the reaction 2.4 takes place in the reactor vessel, the released fusion energy is distributed among products of the reaction - neutron and an α particle. The energy of the α particles can further heat the plasma and thus cover some

of the power losses of plasma medium. Situation, where power losses of plasma medium are fully covered by thermalization of produced α particles is in [13] defined as *plasma ignition*. For quantification of conditions required to reach the ignition of plasma, there are several criterions of which the most commonly used is Lawson criterion. This criterion is equivalent to situation where there is no outer heating of the plasma medium and power obtained by thermalization of fusion α particles exceeds power of losses (caused mainly by Bremsstrahlung radiation). Most common form of the criterion (which can be found in [13]) is represented by following equation:

$$n\tau_E > \frac{12eK_B T}{E_\alpha < \sigma v >}. \quad (2.8)$$

Here, n denotes plasma density, τ_E stands for energy confinement time, E_α is energy of α particles obtained from fusion reaction and K_B is Boltzmann's constant. Finally, $< \sigma v >$ stands for reactivity of D-T reaction (see equation 2.4). The fact that D-T reaction is based on resonance nucleus of ${}^5\text{He}$ causes maximum value of reactivity to be present at lower temperatures than in regular fusion reactions. Criterion in equation 2.8 can be used as the first approximation of the required reactor parameters. Still, it is not absolutely necessary to reach the plasma ignition in order to obtain energetically sustainable reactor. While on one hand [13] states that ignited plasma could be more economically interesting than non-ignited, opposite statements exist as well.

2.4 Confinement

Whether is the 2.8 form of criterion used to describe the ignition conditions, or one of its more accurate engineering forms (an example of one is stated in [6]), the main characteristic of conditions remains as only the parameters on left hand side of the relation 2.8 can be altered. The literature [6] states two priorities of plasma confinement: Firstly to ionize the fuel and heat it to sufficient temperatures. Secondly to confine the fuel long enough to obtain an energy gain. In the present, two most promising concepts of plasma confinement are trying to follow the above-mentioned priorities by polar opposite means to each other.

First approach is to obtain plasma medium of very high density: $\sim 10^{31} - 10^{32} \text{ m}^{-3}$. According to [6], such a dense matter could be obtained by compression of small fuel pellet (less than $\sim 5 \text{ mm}$ in diameter) made of deuterium and tritium. This compression

would be result of subsequent propagation of shock waves, induced by ablation of fuel pellet outer shell. The ablation itself could be caused either by laser beams, X-ray radiation (induced by interaction of lasers with heavy-element material such as *Au*) or by heavy accelerated particles. However, due to large energy contained inside, the fuel pellet will disassemble in form of micro-explosion. Confinement time is thus very short, being $\sim 10^{-8}$ s. Since this confinement concept is based on compression of fuel carried out by propagation of shock waves, it is called *Inertial Confinement Fusion*.

Another approach of Lawson criterion fulfilment is to confine fusion medium of small density $n \sim 10^{21} \text{ m}^{-3}$ for relatively long time $\tau \sim 1 \text{ s}$ (see [6]). Such a long period can be reached by confinement of charged particles of fusion plasma in a strong magnetic field, hence *Magnetic Confinement Fusion*. There are two possible branches of magnetic confinement reactor concept. The first reactor vessel concept is an open magnetic field system, where magnetic field lines confining the plasma leave the reactor vessel. Such a vessel tends to be linear, thus the field lines (and particles) leave reactor on the ends. The more successful concept is of closed magnetic field system, where magnetic field lines stay inside of the vessel and plasma. In following chapters, only a special type of closed magnetic field lines confinement concept is further described.

Chapter 3

Magnetic Field in Tokamak and its Diagnostics

3.1 Tokamak Concept

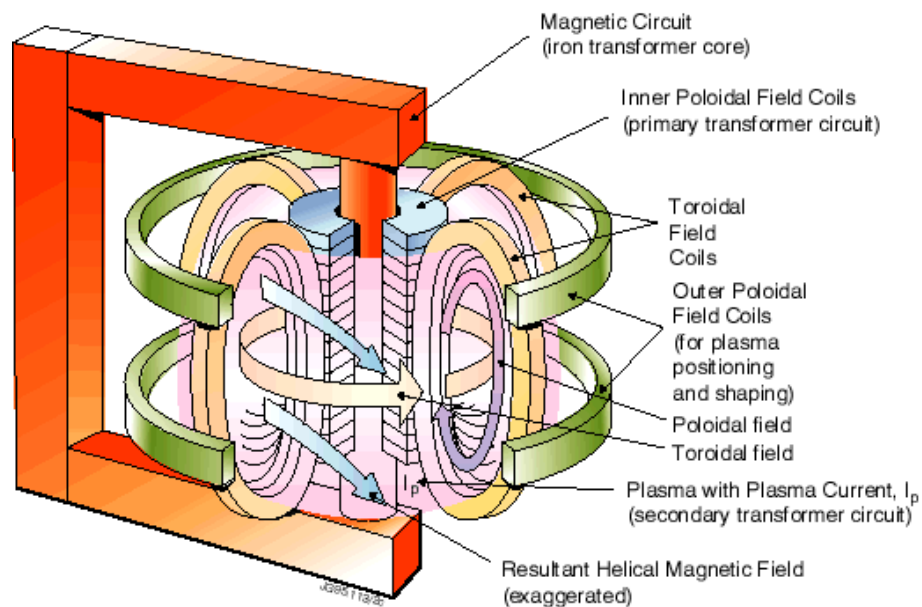


Figure 3.1: Scheme of the tokamak. The figure was obtained from [7].

Among all the magnetic confinement concepts, tokamak is the most advanced one, being closest to reaching the ignition of fusion medium. Scheme of this device can be found in fig. 3.1. Since tokamak is a magnetic confinement device, one of its characteristic features is a system of coils placed around toroidally-shaped chamber. Primary magnetic

field confining plasma inside of vessel is generated by a set of coils encircling chamber of tokamak in poloidal direction (e.g. around the minor axis of the toroid). Such a configuration of magnetic coils results in generation of toroidally-oriented magnetic field (e.g. following minor axis of the toroid), as can be seen in fig. 3.1. However, toroidal field alone proves to be insufficient for a successful plasma confinement, thus an additional poloidally-oriented field has to be implemented (reasons why such a field is necessary are explained in section 3.2). As [22] states, in current tokamak experiments, this field is generated by driving a current through plasma in toroidal direction. Such a current is induced by presence of electric field in toroidal direction, obtained by transformer action. By driving a discharge through inner poloidal field coils depicted in fig. 3.1, a flux change in the center of toroid is induced. This phenomenon can be described with Faraday's law (as in [6]) in following manner:

$$\oint_l \mathbf{E} \cdot d\mathbf{l} = -\frac{d}{dt} \left(\int_{S_t} \mathbf{B} \cdot d\mathbf{S} \right), \quad (3.1)$$

$$E_t = -\frac{1}{2\pi R} \frac{d\psi}{dt}. \quad (3.2)$$

In equation 3.2, topology of tokamak in fig. 3.1 is assumed. E_t stands for toroidal component magnitude of induced electric field, ψ represents the flux through center of the torus and R stands for major radius of the tokamak (the distance between the center of tokamak and the axis of toroidal chamber). Given that flux changes in inner coil and in the center of the tokamak are equivalent (as in transformer), equation 3.2 could be modified:

$$E_t = -\frac{L}{2\pi R} \frac{dI}{dt}. \quad (3.3)$$

In previous equation L stands for inner coil inductance and I represents current driven through this coil. From equation 3.3 it is evident that to obtain a toroidal electric field E_t of constant magnitude, linear change in current driven through inner coil is needed. This limits tokamak to be an impulse device.

As can be seen in fig. 3.1, a set of poloidal magnetic field coils is present in tokamak as well. Field generated by these coils (according to [22]) is used for plasma column position control, being part of dynamic feedback stabilization control.

It is important to note that transformer action does not only generate E_t , but also generates plasma itself by ionization of neutral gas. Additionally, current driven through plasma with high resistivity causes plasmatic column to heat-up. This phenomenon is referred to as *ohmic heating*. However, since resistivity of plasma falls with increasing

temperature, there have to be implemented other means of heating in order to reach fusion temperatures. Literature [22] gives examples of such additional heating systems, ranging from high-energy neutral particle injection to interaction of plasma medium with electromagnetic radiation.

According to [22], current tokamak experiments work with plasma of density $n = 10^{19} - 10^{20} \text{ m}^{-3}$. This values are 6 orders less than atmospheric density, thus it is obvious that high level of vacuum has to be present in chamber of tokamak. Presence of vacuum is also vital in elimination of impurities which, as is stated in [22], would otherwise dilute the fuel and cause critical radiation losses of energy. Since contact of plasma with wall of chamber increases concentration of impurities, it is necessary to either define plasma boundary with material limiter or by modifying magnetic field to get magnetic divertor (see [22]).

3.2 Particle Drifts and Magnetic Field Configuration

As was mentioned in section 3.1, the main magnetic field used for plasma confinement has toroidal orientation. Such a field hinders diffusion of charged particles of plasma in radial direction (outwards from minor axis of toroid). Otherwise these particles would move in direction which is antiparallel to their gradient of pressure (according to [2]), e.g. towards the wall of chamber. However, this field alone is not sufficient for plasma confinement, as it has a non-zero gradient in radial direction (see below). Additionally, although particles in magnetic field are forced to gyrate around its field lines, motion in direction parallel to magnetic field lines is not affected by this field at all. However, toroidal electric field present in chamber is subjecting plasma particles to circular motion along toroidal axis of tokamak. Such a trajectory gives rise to centrifugal forces in direction outwards of vacuum vessel.

According to [2], effect of outer forces on particle trajectories in homogeneous magnetic field can be described as a drift motion. If drift is combined with gyration of particles around magnetic field lines, resultant trajectory can be seen as motion of center of gyration. In literature [2], drift velocity of charged particles subjected to force \mathbf{F} and

placed in magnetic field is expressed as:

$$\mathbf{v}_D = \frac{1}{q} \frac{\mathbf{F} \times \mathbf{B}}{B^2}. \quad (3.4)$$

Centrifugal force $\mathbf{F} = mv_{\parallel}^2 \frac{\mathbf{R}}{R^2}$, to which are particles subjected as they move along curved toroidal magnetic field of tokamak, gives rise to drift dependent on velocity component parallel to magnetic field:

$$\mathbf{v}_{D_1} = \frac{m}{q} v_{\parallel}^2 \frac{\mathbf{R} \times \mathbf{B}}{R^2 B^2}. \quad (3.5)$$

As was mentioned above, toroidal magnetic field on tokamak has a non-zero gradient in radial direction. Presence of such a gradient manifests itself as a force. Drift motion, resulting from such a force can be expressed by following equation by [2] (or by [22] as well):

$$\mathbf{v}_{\nabla B} = \frac{m}{2qB} v_{\perp}^2 \frac{\mathbf{B} \times \nabla B}{B^2}. \quad (3.6)$$

It can be easily proven that decrease in magnitude of magnetic field follows $B \sim \frac{1}{R}$ (example of proof can be found in [2] using Ampere's law in vacuum in cylindrical coordinates). It is thus possible to express gradient of magnetic field induction as: $\frac{\nabla B}{B} = -\frac{\mathbf{R}}{R^2}$. This implies that equation 3.6 can be in this case modified into form of:

$$\mathbf{v}_{D_2} = \frac{m}{2qB} v_{\perp}^2 \frac{\mathbf{R} \times \mathbf{B}}{R^2 B^2}. \quad (3.7)$$

Final equation for particle drifts is obtained by summation of this drift with drift from equation 3.5:

$$\mathbf{v}_D = \mathbf{v}_{D_1} + \mathbf{v}_{D_2} = \frac{m}{q} \left(v_{\parallel}^2 + \frac{1}{2} v_{\perp}^2 \right) \frac{\mathbf{R} \times \mathbf{B}}{R^2 B^2}. \quad (3.8)$$

From equation 3.8 is evident that all the charged particles in plasma will drift vertically. However, since ions and electrons have opposite charge polarity, their respective drift motions will be of opposite direction as well. This will induce additional vertical electric field \mathbf{E} , whose effect on particles will once again manifest itself as a drift, characterized by following equation:

$$\mathbf{v}_{D_E} = \frac{\mathbf{E} \times \mathbf{B}}{B^2}. \quad (3.9)$$

It should be noted that equation 3.9 does not depend on charge anymore. Respective configuration of electric field induced by particle drift in equation 3.8 to toroidal magnetic field (see fig. 3.2), causes all the charged particles of plasma (according to equation 3.9) to drift in direction of increasing \mathbf{R} .

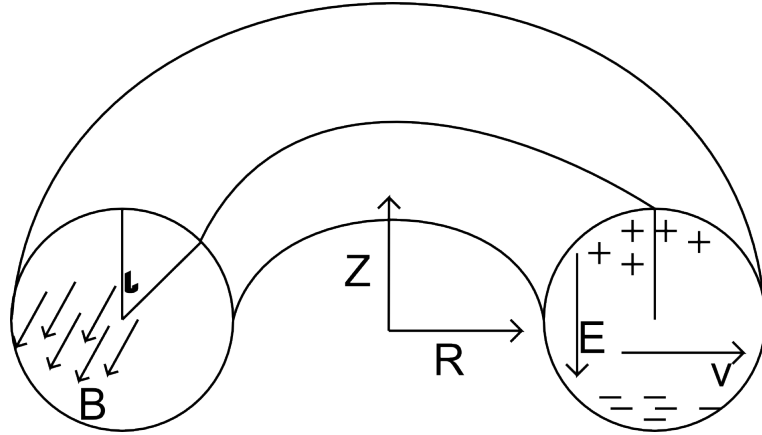


Figure 3.2: Scheme of particle drifts in tokamak. \mathbf{B} stands for toroidal magnetic field, \mathbf{E} for electric field induced by separation of charges due to drift from equation 3.8, hence \mathbf{v} represents drift from equation 3.9. ι denotes rotational transport from equation 3.10.

According to literature [6] and [22], common approach to solve this undesired motion of plasma particles is by introducing a magnetic field of poloidal orientation. By combination of this field with toroidal magnetic field, helically-shaped magnetic field is obtained, as can be seen in fig. 3.1. Gyration centers of particles following magnetic field lines in such a field will rotate around minor axis of the tokamak. Resultantly, even though \mathbf{v}_D drift from equation 3.8 will separate positively and negatively charged particles on opposite vertical sides of chamber (see fig. 3.2), thanks to helical magnetic field lines, these particles will spend statistically the same time on the top and bottom of the chamber. Effect of \mathbf{v}_D drift is thus canceled by averaging. It should be noted that helicity of such a field must not be too strong. According to [4], if this helicity is too strong, plasma can easily become subject to sawtooth perturbations (for more information see [2], [6] or [22]). This can be characterized by *safety factor* q defined as (according to [6]):

$$q = \frac{2\pi}{\iota}. \quad (3.10)$$

Here ι denotes rotational transform of the helical field (see fig. 3.2). For parabolical density profile of plasma column, value of safety factor is increasing with radius from the center of column. It has been experimentally shown that to prevent sawtooth perturbations, condition of $q \geq 1$ in the center of plasma column is necessary. In other words, gyration centers of trapped particles have to complete at least one rotation in toroidal

direction before completing full rotation in poloidal direction. This implies that poloidal magnetic field (and thus current driven through plasma) must not be too strong.

3.3 Magnetic Diagnostics

Magnetic diagnostic system is an inevitable part of overall diagnostic system in fusion experiments. As literature [22] states, by use of conducting loops it is possible to determine plasma current, loop voltage, plasma column shape and position, stored plasma energy and current distribution, although for magnetic field measurements, non-inductive sensors can be used as well.

3.3.1 Rogowski Coil

As one of inductive character sensors, Rogowski coil is based on Ampere's law. A scheme of the coil is depicted in fig. 3.3. In order to measure plasma current, Rogowski coil has to be wrapped around tokamak chamber. According to literature [9], the final equation between the measured current I and voltage U at the ends of the coil can be derived in this manner:

Given that magnetic field induced by current enclosed by Rogowski coil is varying little over one turn of the coil (in the poloidal direction), total flux linkage can be estimated as

$$\phi = n \oint_l \int_S dS \mathbf{B} \cdot \mathbf{dl}. \quad (3.11)$$

Here, n denotes number of turns of the coil per unit length. By use of Ampere's law:

$$\oint_l \mathbf{B} \cdot \mathbf{dl} = \mu I, \quad (3.12)$$

the equation 3.11 takes final form:

$$U = \dot{\phi} = nS\mu\dot{I}. \quad (3.13)$$

From the equation 3.13 it is evident, that in order to obtain I , it is necessary to integrate voltage U . This integration is common trait of all the inductive sensors and is carried out either by analog methods (integration circuits) or by numerical means.

In fig. 3.3 can be seen that conducting wire of coil does not complete its turn around measured current, but is back-winded. This is necessary, because otherwise beside turns

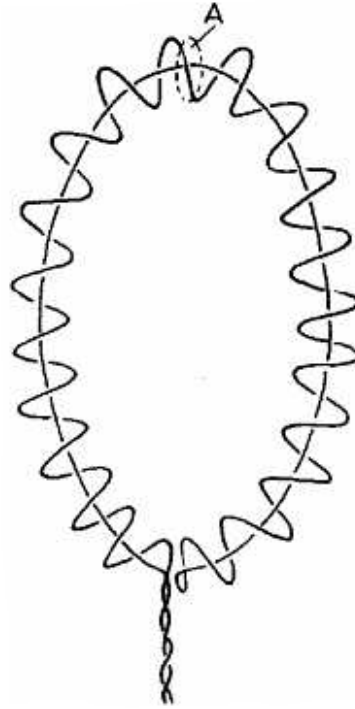


Figure 3.3: Scheme of Rogowski coil from literature [3]. Area A is equivalent to S from equation 3.13.

for current measurement there would also be present a single turn reacting to strong toroidal magnetic field in tokamak.

3.3.2 Magnetic Coil

Magnetic coil is term used for inductive sensor for magnetic field measurement. In literature [3], there are three stated requirements that have to be met, for magnetic coil to become a reliable sensor of magnetic field: sufficient sensitivity to overcome electric noise associated with impulse devices, high frequency response to follow even most rapid fluctuations of measured quantity and finally to have minimal perturbing effect on plasma column (e.g. to be of small size and to be made of appropriate materials). However, these conditions are in conflict with each other, since (according to [3]) in order to rise sensitivity of sensor, effective area of the coil has to rise as well. For better frequency response, this area has to be in configuration of less numerous large loops, rather than large number of small loops. This, however, collides with the requirement of minimal perturbing effect on plasma. It is thus evident that design compromises have to be sought

for the sake of required performance of the sensor.

Even though magnetic coil is used as a magnetic field sensor, it measures rate of change of magnetic induction B (e.g. its derivative) instead of the quantity itself. This is because its principle of operation is based on integral form of Faraday's law (according to [9]):

$$\oint_l \mathbf{E} \cdot d\mathbf{l} = - \int_S \dot{\mathbf{B}} \cdot d\mathbf{S}. \quad (3.14)$$

The closed contour integral can be divided among two integrals - one over the contour of coil and one over the ends of coil:

$$\oint_l \mathbf{E} \cdot d\mathbf{l} = \int_{coil} \mathbf{E} \cdot d\mathbf{l} + \int_{ends} \mathbf{E} \cdot d\mathbf{l}. \quad (3.15)$$

According to [4], in standard experimental configuration is coil implemented into data acquisition system via large impedance, thus no current can be driven in the coil. This implies absence of electric field E , thus first integral on the right-hand side of previous equation has to be equal 0. Literature [9] states other reason why this integral has zero value: By assuming impedance of the coil to be so large, coil can be assumed to be an open circuit. By either way, only the integral over the ends of the coil will have a non-zero value, equal to difference in their potentials. Thus mean value of $\dot{\mathbf{B}}$ can be obtained from equation:

$$V_{in} = -S\dot{B}. \quad (3.16)$$

It is thus evident that voltage V_{in} obtained by the sensor will have to be integrated in order to obtain measured quantity of B . There are two possible means of the integration. Although numerical integration of digitalized data is easier to carry out (by current technological means), analog integration can be used to modify frequency response bandwidth of the coil and thus to enable measurement of larger range of phenomena (according to [19]). According to [16], there are two possible types of integrating circuits. A scheme of passive integrator circuit is to be found in fig. 3.4. According to this scheme, output voltage signal V_{out} can be calculated by following equation (see [16]):

$$V_{out} = \frac{1}{1 + i\omega RC} V_{in} \approx \frac{1}{RC} \int V_{in} dt \quad (\omega RC \gg 1), \quad (3.17)$$

where R stands for resistance and C for capacity. It is evident that this integrating circuit can be used only if condition in equation 3.17 is fulfilled. This however limits the range of frequency bandwidth to higher values, since low frequency signals does not fulfill the condition of $\omega RC \gg 1$. On the other hand, it enables measurement of higher frequencies than it would be possible with given magnetic coil otherwise. Please note, that problem

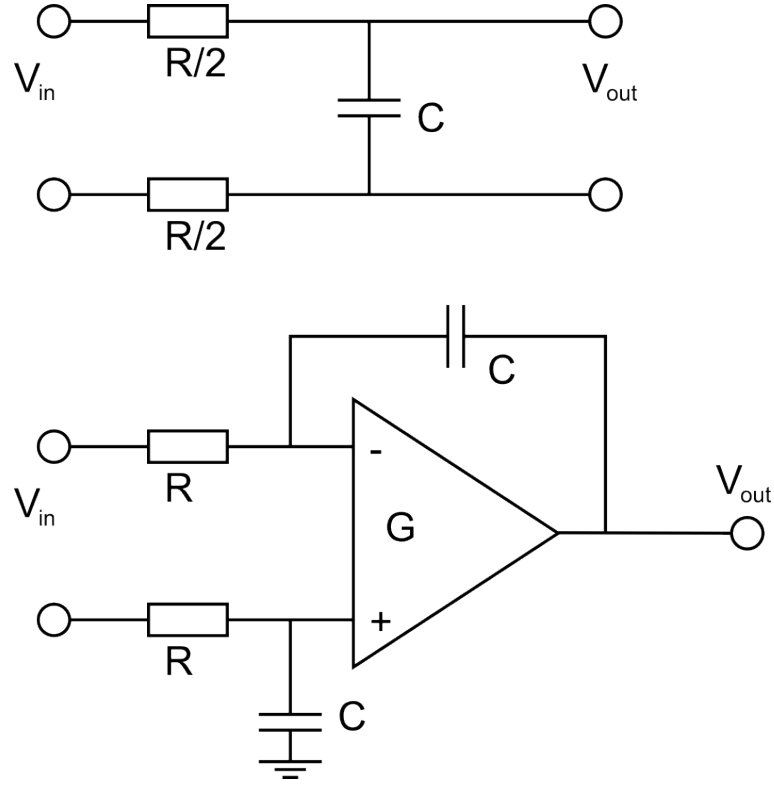


Figure 3.4: Scheme of passive (above) and active (below) integrating circuit from literature [16]. R stands for resistivity, C for capacity and G denotes gain of operational amplifier.

of fulfilling condition in equation 3.17 can not be solved by simply increasing the value of RC product. As can be seen from equation 3.17, this would decrease magnitude of the output signal. However, it is possible to improve integration method by the use of active integrator circuit depicted in fig. 3.4. According to [16], its output voltage can be calculated in following manner:

$$V_{out} = -\frac{G}{1 + i\omega RC + Gi\omega RC} V_{in} \approx -\frac{1}{RC} \int V_{in} dt \quad (G\omega RC \gg 1). \quad (3.18)$$

In this equation, G represents the gain of implemented operational amplifier. It can be seen that approximated form of previous equation is equivalent to the one in equation 3.17. However, there is difference in condition of approximation. According to [16], as values of G are of orders 10^5 , it is evident that active integrator allows magnetic field measurements even on timescales 1 - 10 s. On the other hand, literature [16] states that there is a serious problem with "integrator drift" in obtained signal if an active integrator is used for its integration, since any constant offset on the input will be integrated as well.

This flaw in design can be solved by implementation of even more complex circuits into the integrator. More information concerning these methods can be found in literature [16] and [19].

By integration is signal from magnetic coil in form of V_{in} converted into V_{out} , which is recorded by data acquisition system. Equation 3.16 is can be thus modified into final form of:

$$B = \frac{RC}{S} V_{out}. \quad (3.19)$$

3.3.3 Poloidal Flux Loop

This sensor serves the purpose of loop voltage measurement for plasma conductivity evaluation (see [9]), as well as for purposes of plasma position control and equilibrium reconstruction (see [16]). As an inductive sensor, it is based on Faraday's law, similarly to magnetic coil from section 3.3.2. One or more flux loops are encircling vacuum vessel of tokamak from the outside in order to measure voltage induced by transformer action (see section 3.1 or literature [9]). As toroidal electric field is generated inside of the chamber, the same field is induced in conductive flux loop. Resultantly, on both the plasma column and flux loop ends, a difference in potential of the same magnitude is generated. This voltage is then directly measured by flux loop. By integration of this voltage, a poloidal flux can be evaluated.

3.3.4 Hall Probes

As was explained in section 3.3.2, there are many technical difficulties in measurements of magnetic field by coils. All the problems with frequency response and signal integration could be avoided by use of sensors based on different principle of operation. One of the most promising alternatives is the use of special galvanometric sensors called Hall probes. Measurement of magnetic field by Hall probes is based on physical phenomenon called Hall effect, named after physicist Edwin H. Hall. By assuming configuration depicted on fig. 3.5 this physical phenomenon can be explained (according to [11]) as follows:

Motion of individual trajectories of charged particles is subjected to Lorentz force. Considering plate of semiconductor (as in fig. 3.5), it is evident that in absence of outer magnetic field B the only motion of charged particles is drift motion between contacts

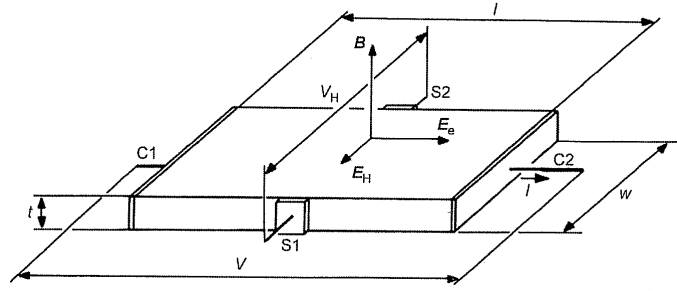


Figure 3.5: Figure from literature [11] of Hall plate. $C1$ and $C2$ are contacts for implementation of external current I , while $S1$ and $S2$ are contacts for measurement of induced Hall voltage V_H . Dimensions of the plate are characterized by w , l and t . Outer magnetic field induction is represented by B

$C1$ and $C2$, induced by external field \mathbf{E}_e , given by following equation (see [11]):

$$\mathbf{v}_d = \mu \mathbf{E}_e. \quad (3.20)$$

Here μ represents mobility of the particles. Take note that by taking effect of collisions into consideration, constant velocity instead of accelerated motion was obtained. Introducing magnetic field \mathbf{B} will result in drift motion of charged particles between contacts $S1$ and $S2$. Resultantly, Hall electric field \mathbf{E}_H is induced. By taking linear dependency of drift velocity and electric field into consideration, following equation is obtained:

$$\mathbf{E}_H \sim \mu \mathbf{E}_e \times \mathbf{B}. \quad (3.21)$$

To be exact, previous equation describes only one component of charged particles motion, that is component of drift induced by magnetic field. This drift is perpendicular to major drift of particles in direction of main electric current. To fully characterize the motion of particles, vectors of both of the drifts have to be considered. By expressing intensity of electric field by voltage, equation for Hall voltage V_H is obtained in form:

$$V_H \sim \mu \frac{w}{l} V B. \quad (3.22)$$

It can be thus seen that measured Hall voltage V_H is directly proportional to measured magnetic field and no integration is needed.

According to [11], characteristic dimensions of Hall plates are roughly $t = 10 \mu m$ thick, $w = 100 \mu m$ wide and $l = 200 \mu m$ long. Thus they are often integrated into chips.

Advantages of Hall transducer being integrated into chip are (according to literature [5]) as follows: stabilization of the supply voltage, output amplification, high-frequency noise suppression and elimination of dependency on environment temperature. On the other hand, [16] states that radiation damage is of great issue in Hall probes. Despite that, the same literature states that Hall probes might be feasible at least for experiments of the scale equivalent to ITER.

Chapter 4

Tokamak GOLEM

4.1 Overall Characteristics



Figure 4.1: Present status of tokamak GOLEM. Tokamak itself is on the left panel while room for containment of energizing systems is on the right panel.

Tokamak GOLEM plays an important role in Physics and Technology of Thermal Fusion curriculum of Faculty of Nuclear Sciences and Physical Engineering (part of Czech Technical University). According to [12], this tokamak was originally called TM-1-MH and used to be stationed in Kurchatov Institute in Moscow. In 1977 the device was transferred to Institute of Plasma Physics in Prague. After the vacuum vessel underwent a reconstruction in 1984, the device was renamed to CASTOR (Czech Academy of Sciences TORus). Tokamak obtained its final form in 1988, when feedback plasma position control was installed. After the Institute of Plasma Physics obtained tokamak COMPASS-D



Figure 4.2: A sample from liner replaced in 1984, encircled by coil of toroidal magnetic field generation.

from research center in Culham, CASTOR tokamak was given as a gift to Faculty of Nuclear Sciences and Physical Engineering in winter of 2007, where is presently stationed and called GOLEM. As can be seen in fig. 4.1, tokamak itself is placed in a specially prepared room, while energizing systems and part of vacuum system are placed in cellar. Engineering scheme of the tokamak can be found in fig. 4.3.

Having major radius $R = 0.4 \text{ m}$ and minor radius $a = 0.085 \text{ m}$ (in this case, minor radius denotes limiter radius, see [10] or [21]) both with circular cross-section, tokamak GOLEM falls under category of small tokamaks, as defined in literature [10]. Chamber of this tokamak is made of two parts. Innermost layer, containing plasma column and (called *liner*), is enveloped by outer coating made of copper. According to [21], the copper layer is 10 mm strong, having toroidal shape with of major radius $R_c = 0.4 \text{ m}$ and minor radius of $a_c = 0.115 \text{ m}$. Coating is vertically divided into two parts by electrical insulation in order to prevent making a conducting loop in coating. Also, to enable permeating of magnetic field through the coating, there is a horizontal cut present as well (see [1]). Having six diagnostic ports, literature [20] and [21] states that theoretically, 14% of plasma length is not shielded. Additionally it was experimentally shown in [20] that this value is most likely higher. Similarly to coating, liner is in shape of toroid as well, having major radius $R_L = 0.4 \text{ m}$ and minor radius $a_L = 0.1 \text{ m}$. However, unlike coating, it is not divided with insulation, nor has any cuts except for diagnostic entries and thus makes a conducting loop. The whole liner is made of bellows stainless steel, commonly used in vacuum systems (see fig. 4.2). In this tokamak, boundary of plasma is defined by material limiter of circular shape made of molybdenum and placed on 0.085 m radius (according to [1]).

As can be seen in fig. 4.3, vacuum system is two-staged. Pre-vacuum inside of liner is obtained by use of oil rotary pump located in cellar. In order to obtain level of vacuum

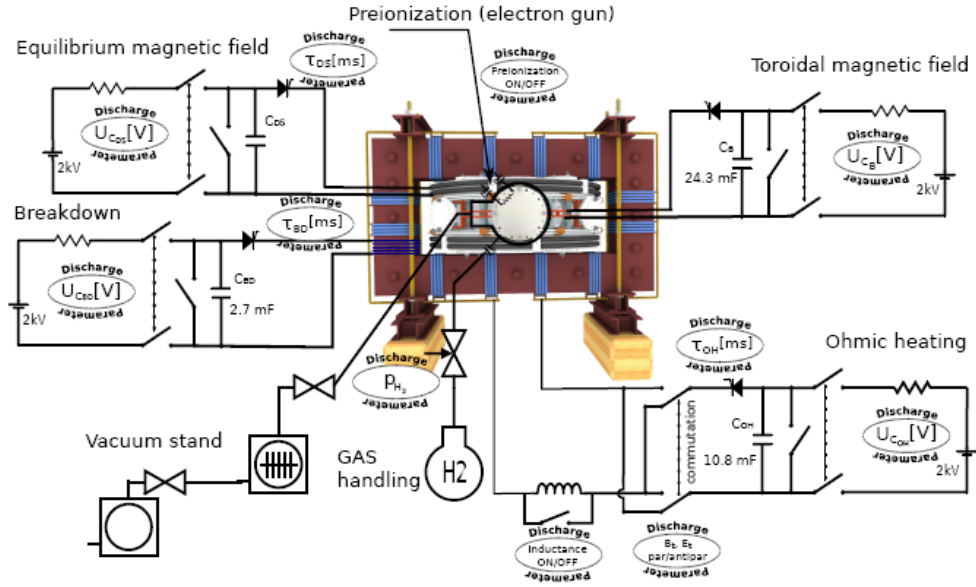


Figure 4.3: An engineering scheme of the tokamak GOLEM, obtained from [18].

required for generation of plasma, turbomolecular pump has to be implemented as well. According to [18], this system enables to obtain background pressure of values $\sim 0.5 \text{ mPa}$. Density of particles at room temperature can be thus estimated (with simple calculation of $n = p/K_B T$) to be $n \sim 10^{17} \text{ [m}^{-3}\text{]}$. Plasma is generated of H_2 work gas injected into the liner vacuum. Pressure of work gas inside can be regulated in scales of $10 - 200 \text{ mPa}$. Additionally, in order to obtain higher levels of vacuum, there is implemented system for baking of the tokamak (as a wall conditioning) and glow discharge cleaning (see [18]). Before the discharge of toroidal electric field capacitors takes place, work gas is pre-ionized with an electron gun, in order to help the generation of plasma. According to [1], electron gun is represented by directly heated wolfram wire of negative potential to liner, placed behind limiter radius.

All the experiments on tokamak GOLEM are triggered and controlled by PC. There also exists possibility of remotely handled experiment from abroad (more information concerning the issue can be found in [18]). It is therefore natural that all the measured experimental data are in digital form and accessible via the internet. The acquisition of all these data is done by two independent systems, as can be seen in fig. 4.8. While basic data-acquisition system (in fig. 4.8 named as *DAS 1*) specializes in basic parameters of discharge, National Instruments' data-acquisition system (named as *DAS 2*), with its

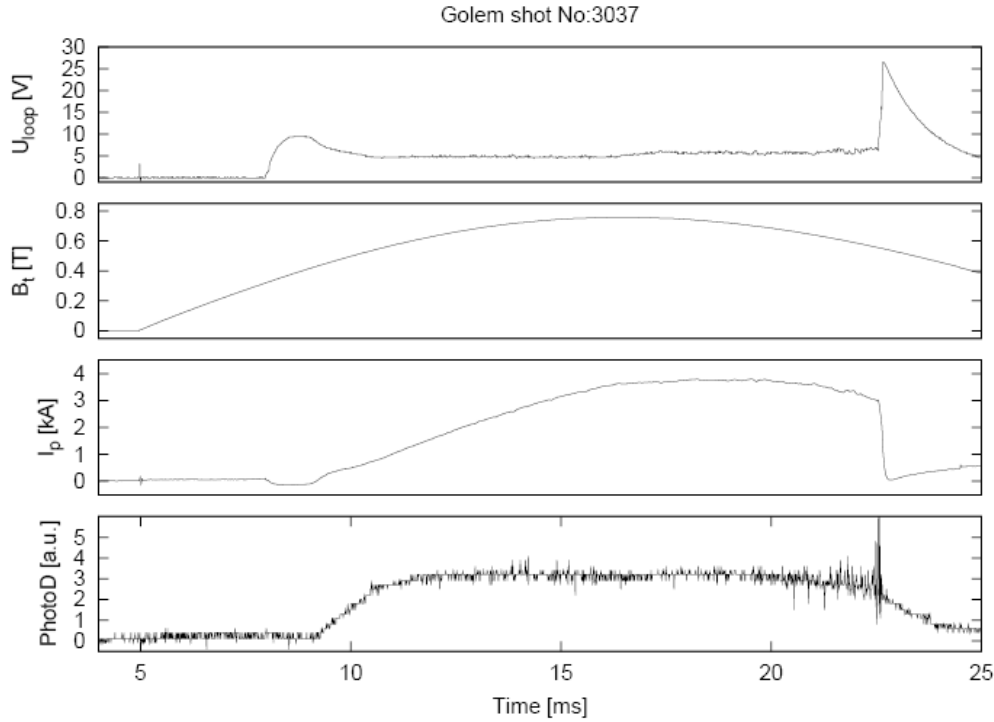


Figure 4.4: An example of typical evolution of basic measured parameters. U_{loop} stands for loop voltage, B_t represents toroidal magnetic field, I_p is current of plasma and $PhotoD$ is signal from photodiode measuring radiation from chamber on wavelengths of visible light. In the case of interest, analysis of this shot can be found in [18].

numerous channels enables measurement of any additional parameters needed in given experimental arrangement. For their mutual consistency, both of the systems are synchronized to sampling frequencies of 100 kHz . An example of data obtained by *DAS 1* system, describing typical evolution of basic parameters of plasma and tokamak, can be found in fig. 4.4.

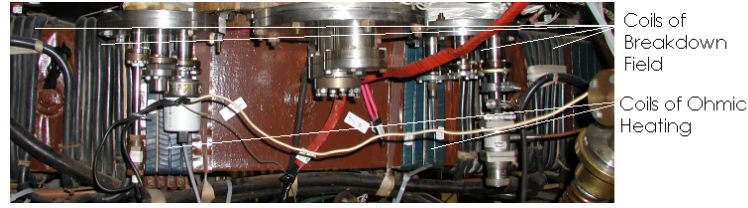


Figure 4.5: Coils of toroidal electric field generation.



Figure 4.6: Coils of toroidal and poloidal magnetic field generation.

4.2 Configuration of Electric and Magnetic Fields

4.2.1 System of Toroidal Electric Field Generation

As was explained in section 3.1, toroidal electric field is generated by change of magnetic flux along the main axis of tokamak. On tokamak GOLEM, this field is generated by two independent systems of magnetic coils encircling the limbs of its transformer. One set of coils is used for plasma breakdown, while the one other is used for purposes of driving the current through plasma and for ohmic heating. Locations of the coils are depicted in fig. 4.3 and 4.5. Each set of coils is energized by system of capacitors of its own. According to [18] (also can be seen in fig. 4.3), plasma breakdown field capacitors have capacity of $C_{BD} = 2.7 \text{ mF}$ being charged to 400 V . Capacitors of ohmic heating current drive are represented by capacity of $C_{OH} = 10.8 \text{ mF}$ and charged to 400 V . According to [18], these capacitors are capable of generating plasma current of magnitude $< 8 \text{ kA}$. In order to prolong discharge of these capacitors, an additional inductance $L = 5.9 \text{ mH}$ is implemented into corresponding system (see fig. 4.3). In both the coil systems it is possible to choose polarity of current from capacitors, thus there are two possible polarities of induced electrical fields.

4.2.2 System of Toroidal Magnetic Field Generation

Toroidal magnetic field of tokamak GOLEM is generated by set of 28 copper coils, homogeneously distributed around the coating. According to [1], each of the coils is made of copper layer with 8 turns in total and placed in aluminium coating (see 4.2 and 4.6). Literature [18] states that coils are energized by capacitor system of $C_B = 24.3 \text{ mF}$, which can be charged up to 2 kV . In an example of generated magnetic field in fig. 4.4 it can be seen that magnitude of generated field varies over the time of plasma discharge. This is one of specific traits of tokamak GOLEM, since according to [3] in the larger tokamaks the magnitude of toroidal field is kept constant in times of plasma duration. Similarly to systems of electric field generation, polarity of discharge (and thus direction of generated field) can be changed in this capacitor system as well.

4.2.3 System of Stabilization Magnetic Field Generation

Stabilization magnetic field coils played vital part in feedback plasma position control on tokamak CASTOR, as they generated the compensation poloidal magnetic field. Even though dynamic feedback is not yet operational on tokamak GOLEM, a set capacitors (which can be charged up to 1 kV , according to [18]) is dedicated for purposes of energizing one of the compensation windings. Locations of the quadrupole coils, together with directions of currents driven through them, are described in fig. 4.7. Coils placed ex-vessel of the tokamak can be distinguished by color of their insulation and number of bends. While horizontal field generation coils are purple and have 4 bends, coils of vertical field generation are black with 2 bends.

4.3 Magnetic Diagnostics

It is safe to assume that magnetic diagnostics are currently the most significant diagnostics on tokamak GOLEM, since they are used to measure basic parameters of plasma. Even though almost all the sensors used for magnetic diagnostics on tokamak GOLEM are the same that were used on tokamak CASTOR, there is one significant difference in processing of their data. Namely, while on tokamak CASTOR were signals of inductive sensors integrated by analog means, currently on tokamak GOLEM are all such data integrated numerically. This difference will be further discussed in section 4.3.3. An

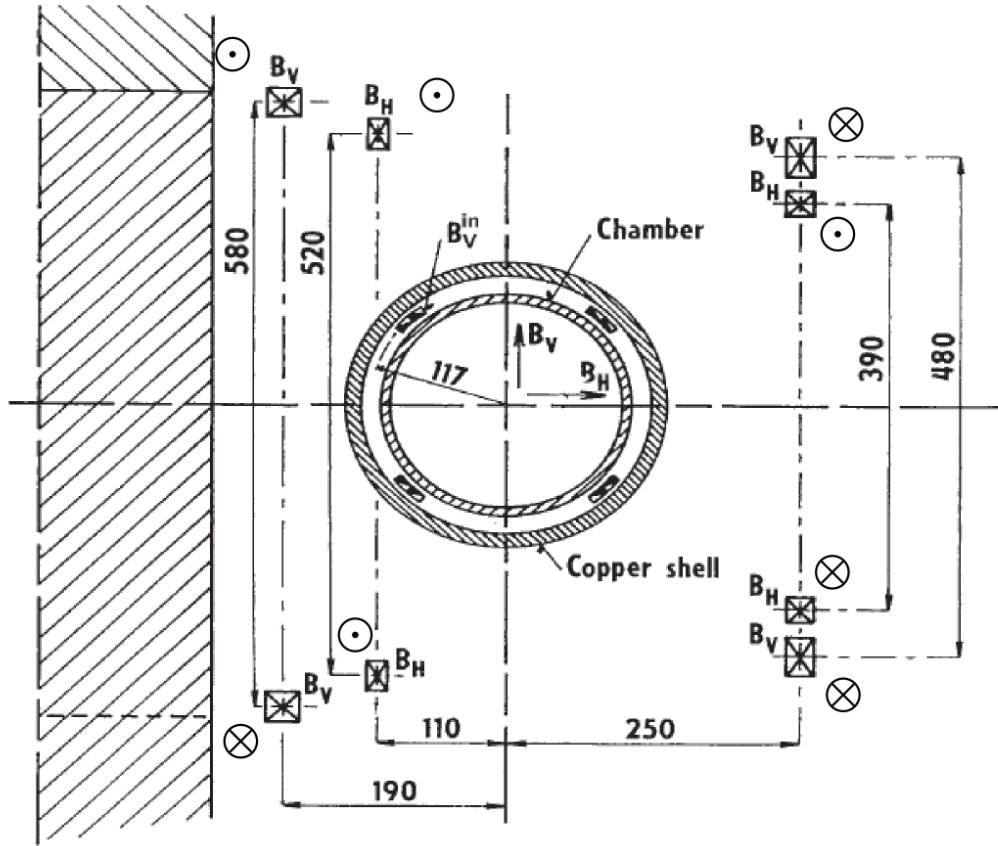


Figure 4.7: Scheme of compensation windings with corresponding polarities of currents. B_H stands for coils of horizontal stabilization field generation, B_V denotes coils of vertical field and B_V^{in} represents coils of vertical field, placed under the coating. Scheme can be found in literature [3], while configuration of currents is described in [1].

overview of presently used magnetic diagnostics, can be found in fig. 4.8.

4.3.1 Rogowski Coils

For purposes of current measurements, there are two Rogowski coils used on tokamak GOLEM. While large Rogowski coil is encircling the chamber of tokamak in order to measure plasma current, small Rogowski coil is used to measure currents flowing through other, smaller conductors. Large coil can be seen in fig. 4.9, while the small one is in fig. 4.10. Principle of their operation can be found in chapter 3.3.1. Main characteristics

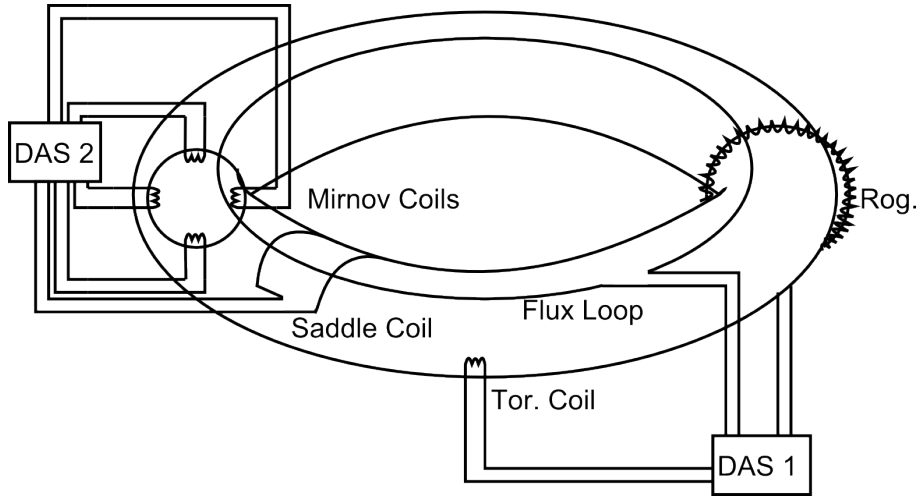


Figure 4.8: Scheme of present magnetic diagnostics of tokamak Golem with their respective data acquisition systems. *Rog* stands for Rogowski coil described in section 4.3.1, *Flux Loop* is described in section 4.3.2, *Tor.Coil* stands for sensor from section 4.3.5 and *Saddle Coil* is described in section 4.3.4. Finally, *Mirnov Coils* are described in section 4.3.3. *DAS 1* and *DAS 2* denote data acquisition systems described in section 4.1.

of large coil are summarized in tab. 4.1 (accordingly to [23]). From equation 3.13, value of its calibration constant can be calculated to be $5.4 \cdot 10^6 \text{ AV}^{-1}\text{s}^{-1}$. Calibration constant K_1 in tab. 4.1 was stated in [23] to be the actual value, determined by empirical means. Similarly to that, calibration constant of small Rogowski coil is stated in [24] to be $K_2 = 6.55 \cdot 10^6 \text{ AV}^{-1}\text{s}^{-1}$.

4.3.2 Flux Loops

Unlike other magnetic diagnostics sensors, flux loops used on tokamak GOLEM are not the ones that were used on tokamak CASTOR. For purposes of flux voltage measurements, two conducting wires are placed on the top of the chamber, as can be seen in fig. 4.9. For more information about their operation see section 3.3.3. Event though loop on smaller radii is used only sporadically, loop on larger radii is constantly implemented into *DAS 1* system, being part of basic plasma parameters diagnostics.

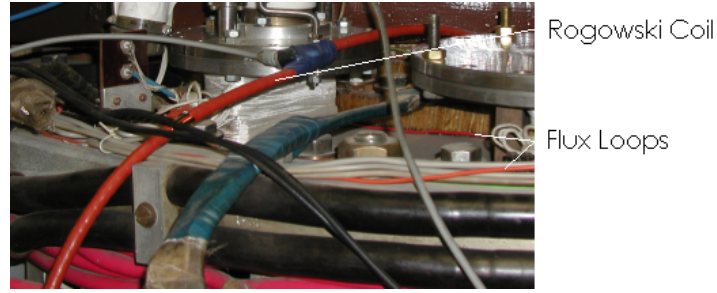


Figure 4.9: Figure of large Rogowski coil encircling vacuum vessel of tokamak and both of the flux loops together.



Figure 4.10: Small Rogowski coil used for measurement of currents flowing through conductors.

4.3.3 Mirnov Coils

On tokamak GOLEM (and formerly on CASTOR as well), Mirnov coils is term used for small coils of local poloidal magnetic field measurement, placed inside of liner. Basic principles of magnetic field measurement using coils are explained in section 3.3.2. The main purpose of Mirnov coils is to determine the position and movement of plasma column inside of liner (method will be explained in chapter 6). According to [15], all the coils are the same, with their characterization summarized in tab. 4.2. In [15], effective area of the coils can is evaluated as:

$$S_{eff} = N\pi\left(\frac{D_{outer} + D_{inner}}{4}\right)^2 = 3705 \text{ mm}^2. \quad (4.1)$$

Each of the coils is enveloped by a ceramic cylinder made of porolite, for protection from plasma particles, as these coils are placed on a circular rack, put inside of liner. Their spatial configuration can be seen in fig. 6.1. As is mentioned in [15], coils are placed on minor radius of 93 mm. Although Mirnov coils are used for measurement of poloidal

l	230 <i>cm</i>
D_{wire}	0.3 <i>mm</i>
D_{inner}	7.9 <i>mm</i>
n	$3 \cdot 10^3 \text{ m}^{-1}$
K_1	$5.3 \cdot 10^6 \text{ AV}^{-1}\text{s}^{-1}$

Table 4.1: Characterization of large Rogowski coil. l denotes overall length of the coil, D_{wire} is the diameter of wire of the coil and D_{inner} the diameter of the coil itself. n represents number of turns of the coil per unit length and K_1 stands for calibration constant.

L	14 μH
R	1.055 Ω
D_{wire}	0.34 <i>mm</i>
D_{inner}	6.0 <i>mm</i>
D_{outer}	8.4 <i>mm</i>
N	91

Table 4.2: Characterization of Mirnov coils. L denotes inductance, R stands for resistance, D_{wire} denotes the diameter of the wire of the coil, N stands for total number of turns in each coil. There are two layers of turns with diameters D_{inner} and D_{outer} respectively.

field, due to their misalignment they pick-up the cross-talk from toroidal magnetic field as well. Method of toroidal field cross-talk elimination is described in section 6.2.

It was mentioned before that in present, none of the inductive sensors on tokamak GOLEM is integrated by analog means. However, as can be seen from tab. 4.2, small radius of Mirnov coils and relative large number of turns imply (see section 3.3.2), that their frequency response might be too slow to follow fast fluctuations of plasma. In fig. 6.2 (chapter 6) there can be seen an example of numerically integrated data obtained from one of the coils, where the problem with slow response of coil is evident. Should the data of Mirnov coils be integrated analogically, there is a high probability that observed response rate problems would not develop. In literature [21] there is implicitly stated that on tokamak CASTOR, the data from Mirnov coils were integrated by the use of an active integrator (as the one in fig. 3.4). Even though literature [21] does not further explain

the scheme of used integrated circuit (though all the active integrators are principally of the same design) nor does it give any information on used amplifiers, it clearly states $R = 12\text{ k}\Omega$ and $C = 0.1\text{ }\mu\text{F}$ giving product of $RC = 1.2\text{ ms}$. Since passive integrators are very effective on higher frequencies (e.g. where the Mirnov coils have difficulties following the signal), there exists possibility that for present experimental needs on tokamak GOLEM, a simple passive integrator depicted in fig. 3.4 (with its values of R and C equivalent to the ones above) would be sufficient. Even though passive integrators are not suitable for tokamaks with long pulses, since on tokamak GOLEM pulses are of several tens of ms, there is high probability that there will not be any problems with following the signals at lower frequencies.

By simple measurement, it can be determined whether the used integrator manages to follow all the signals or not. First of all, please take note that signals of question are the ones of slow processes such as toroidal magnetic field generation, since passive integrator does not have problems following fast processes such as perturbations. Most of Mirnov coils are misaligned, thus at vacuum shots, their integrated signals follow the shape of toroidal magnetic field evolution. By comparison of vacuum shot signals of one coil integrated analogically and one integrated numerically, the same shape of signal should be obtained. Finally, please take note that coil *MC13* is not suitable for this control measurement, as its misalignment is not detectable (see tab. 6.1).

4.3.4 Saddle Coil

Term saddle coil comes from the characteristic shape of this coil, placed on the top of the chamber similarly as a saddle would be (see fig. 4.8). Despite its unusual shape, principle of its operation is equivalent to the one of standard magnetic coil (described in section 3.3.2). Saddle coils on tokamaks are used for purposes of plasma column position determination by measuring local vertical magnetic field. More information concerning role of saddle coil in plasma position diagnostics can be found in chapter 6. On tokamak GOLEM, this coil is placed below the copper coating, thus it is very hard to access and calibrate.

4.3.5 Toroidal Magnetic Field Measurement Coils

For toroidal magnetic field measurements on tokamak GOLEM, two magnetic coils can be used. Namely a large coil consisting of a single loop of conductor encircling the liner,

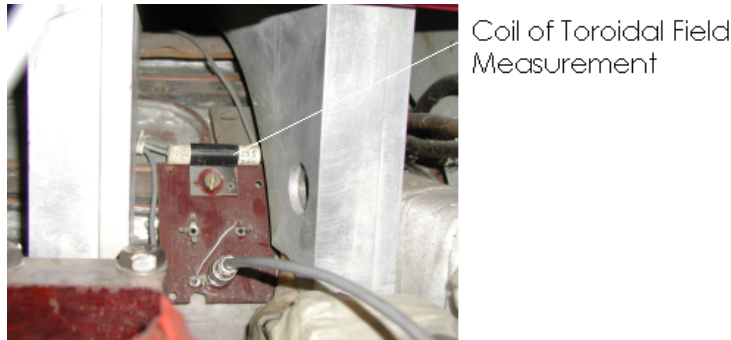


Figure 4.11: Small coil used for toroidal magnetic field measurement.

and a small coil (see fig. 4.11) placed on low-field side of the chamber. While large loop can be used for measurement of average toroidal magnetic field inside of liner, small coil is designated to measure local toroidal magnetic field on low-field side of the tokamak. [23] states, that radius of large loop is equivalent to 0.145 m while small coil is made of conductor of 5 mm radius with 255 turns in total. Please note that since toroidal magnetic field evolution is a relatively slow process, there is no need for any of these coils to have high frequency rate of response (thus numerical integration is sufficient). As can be seen in fig. 4.11, exact poloidal and radial coordinates of small coil would be difficult to estimate. Thus, the small coil was calibrated with the use of large loop. According to [23], it was measured that sensitivity of small coil towards average toroidal magnetic field is 5.98 - 6.06-times lower than the sensitivity of the large loop. This implies that effective area of small coil is 6-times lower than the one of the loop. Thus, effective area of small coil, reacting to average field, is equal to $11 \cdot 10^{-3}\text{ m}^2$. By division of integrated voltage signal with this constant, a magnitude of average magnetic field is obtained. This enables to measure average magnetic field in liner with small coil as well. Please note that this calculated effective area is not equivalent to the real effective area of the coil (being equal to $20 \cdot 10^{-3}\text{ m}^2$) corresponding to local magnetic field measurement.

4.3.6 Hall Probes

Hall probes are different to all the mentioned magnetic diagnostics on tokamak GOLEM so far, as principle of their operation is not based on induction, but on galvanometric effects of semiconductors (see section 3.3.4) and thus their signal does not need to be integrated. Although Hall probes are not presently used on tokamak GOLEM, they have assisted in several experiments on this tokamak before as sensors of local poloidal

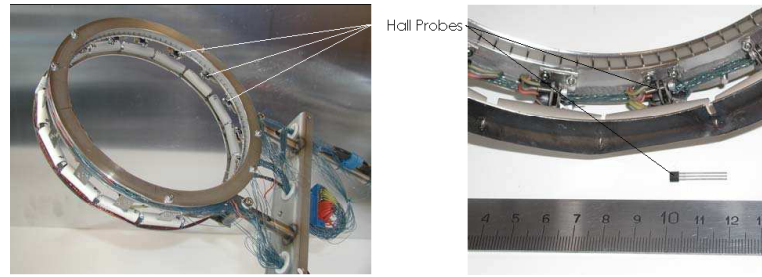


Figure 4.12: A diagnostic ring with Hall probes. Image was obtained from [5].

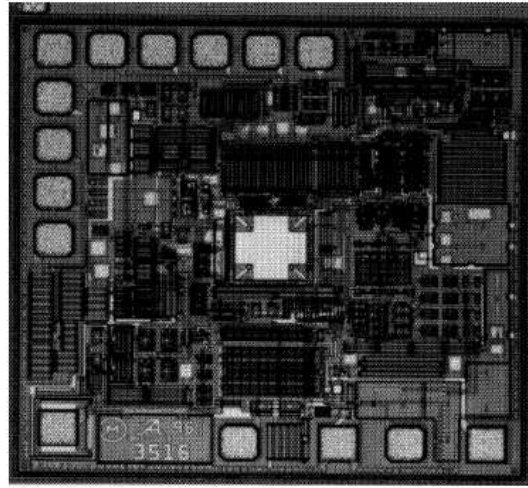


Figure 4.13: Allegro A1322LUA type chip with integrated Hall transducer in the center. Image can be found in [14].

magnetic field. In chapter 5 there is shown that there is very good consistency between Hall probes and Mirnov coils, thus there exists possibility that Hall probes could be able to replace Mirnov coils altogether in the case that problem of slow frequency response of Mirnov coils could not be solved. As can be seen in fig. 4.12, Hall probes are relative small and mounted on a ring of stainless steel with radius of 95 mm (as stated in [5]). There are 8 operational probes mounted on the ring altogether (according to [4]), and their configuration enables to measure both horizontal and vertical poloidal magnetic field on the top, bottom, low-field side and high-field side of the tokamak. Used Hall effect sensors are in form of integrated chips (list of sensor chip integration advantages can be found in section 3.3.4), as can be seen in figs. 4.12 and 4.13. The used type of sensor is the one of *A1322LUA*, produced by Allegro Microsystems Inc. In literature [5] and [14], basic

T_{oper}	-40 °C - 150 °C
f	30 kHz
K_{sens}	31.25 mV/mT \pm 1.56 mV/mT
V	5.0 V

Table 4.3: Properties of integrated circuits of Hall probes. T_{oper} stands for interval of operating temperature, f is maximal frequency of the signal. K_{sens} stands for nominal sensitivity of the single integrated sensor. V denotes supply voltage of each sensor.

properties of the sensors (which can be found in tab. 4.3) are summarized. Calibration of the ring can be done by Helmholtz coil and an example of calibration results can be seen in section 5.2 in table 5.1.

Chapter 5

Modeling and Measurement of Poloidal Magnetic Field

In the case of shot with no plasma on tokamak GOLEM, the inside of liner behaves as a vacuum without any conductive elements and with relative permeability of environment equal to 1. However, it is not clear to what extent can be this assumed of material between the inside of liner and coils of poloidal magnetic field (the ones placed outside of chamber). Investigation of this problem was carried out by measurement of poloidal magnetic field magnitude present inside of liner, which was generated by poloidal field coils placed ex-vessel of tokamak.

5.1 Numerical Evaluation of Magnetic Field Induction by Use of Biot-Savart's Law

For analytical purposes of magnetic induction \mathbf{B} evaluation in simple magnetic field configurations, Ampere's law is commonly used. However, in order to numerically evaluate magnitudes of all the \mathbf{B} vector components, more specific forms of Ampere's law have to be used in calculation. One such a form named Biot-Savart's law is stated in literature [17]:

$$\mathbf{B} = \frac{\mu_0}{4\pi} I \oint_l \frac{d\mathbf{l} \times \mathbf{R}}{|\mathbf{R}|^3}. \quad (5.1)$$

In previous equation, \mathbf{R} represents relative distance between the fixed point in space (where the \mathbf{B} is evaluated) and the respective length element $d\mathbf{l}$. If evolution of current

I driven through conductors generating the magnetic field is known, numerical evaluation of integral enables to determine evolution of all the components of \mathbf{B} vector. Please note that in equation 5.1, environment is assumed to be vacuum, hence μ_0 . The numerical evaluation of \mathbf{B} was done by IDL programming language (similar to Matlab) with algorithm described below:

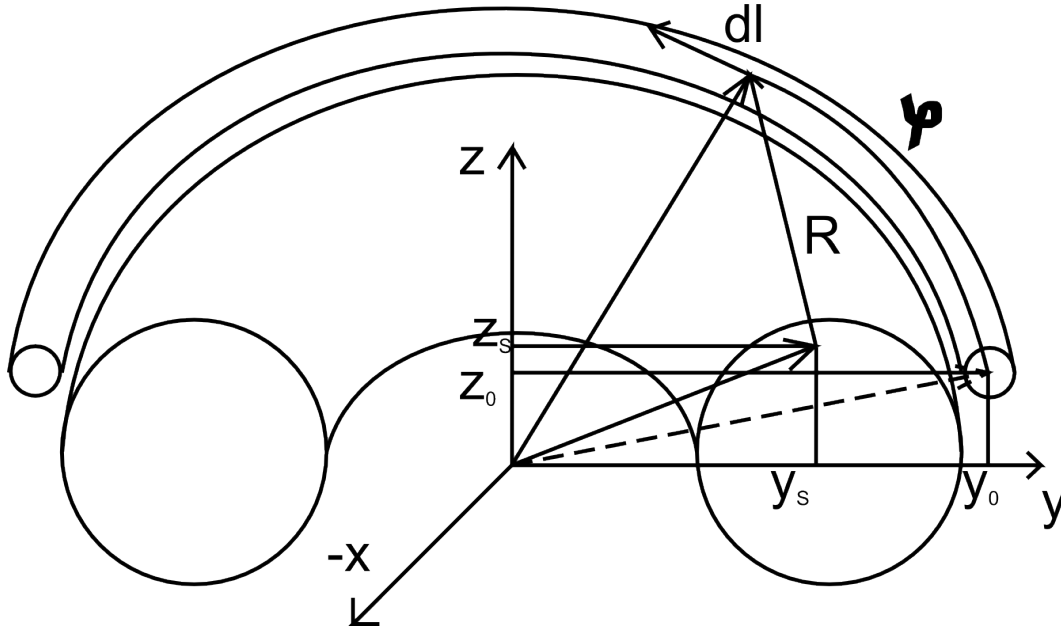


Figure 5.1: Scheme for purposes of algorithm explanation. Location of sensor (e.g. place where \mathbf{B} is being calculated) is represented by vector with full line and corresponds to coordinates $[y_s; z_s]$. Coil generating \mathbf{B} is in given poloidal plane represented by dashed vector with coordinates $[y_0; z_0]$. Element of coil, whose contribution to \mathbf{B} is calculated, is connected with center of coordinate system by a full line vector. Relative distance between the sensor and this element (of length dl) is represented by full line vector denoted \mathbf{R} . φ stands for toroidal angle. Please note that axis x is inverted.

For purposes of numerical evaluation of magnetic field induction \mathbf{B} , configuration in fig. 5.1 was assumed. The integral in equation 5.1 was calculated as a sum of contributions of $10^5 dl$ elements. Thus coil had to be divided into equivalent number of parts. To achieve this, 10^5 equidistantly distributed nodes were put into closed interval of $\langle 0; 2\pi \rangle$. As in each node respective values of sine and cosine were calculated, two large arrays of sine and cosine were obtained. Similarly, length of element of coil was defined as $dl = 2\pi y_0 / 10^5$.

From fig. 5.1 it is evident that components of \mathbf{R} vector can be calculated as:

$$\mathbf{R}_x = y_0 \sin(\varphi[i]), \quad \mathbf{R}_y = y_0 \cos(\varphi[i]) - y_s, \quad \mathbf{R}_z = z_0 - z_s. \quad (5.2)$$

Here $\varphi[i]$ stands for angle corresponding to toroidal location of calculated element. Similarly, vector $d\mathbf{l}$ is expressed as:

$$d\mathbf{l}_x = dl \cdot \cos(\varphi[i]), \quad d\mathbf{l}_y = dl \cdot \sin(\varphi[i]), \quad d\mathbf{l}_z = 0. \quad (5.3)$$

Since the \mathbf{B} vector generated by assumed coil has only poloidal component, $B_x = 0$, while other two components can be calculated by following expressions:

$$B_y = \frac{\mu_0}{4\pi} IdlN \sum_{i=1}^{100000} \frac{(z_s - z_0) \cos(\varphi[i])}{[(y_0 \sin(\varphi[i]))^2 + (y_0 \cos(\varphi[i]) - y_s)^2 + (z_0 - z_s)^2]^{\frac{3}{2}}}, \quad (5.4)$$

$$B_z = \frac{\mu_0}{4\pi} IdlN \sum_{i=1}^{100000} \frac{(y_0 \cos(\varphi[i]) - y_s) \cos(\varphi[i]) + y_0 \sin^2(\varphi[i])}{[(y_0 \sin(\varphi[i]))^2 + (y_0 \cos(\varphi[i]) - y_s)^2 + (z_0 - z_s)^2]^{\frac{3}{2}}}, \quad (5.5)$$

where N stands for number of turns of coil. Please take note that all the values of constants and vector components were defined to be double precision numbers in the calculating program.

In order to determine precision of calculation, this algorithm was used to compute magnitude of \mathbf{B} in a configuration of coil that could be solved analytically as well. For this purpose, a single loop of conductor of radius r was assumed. By driving current I through such a loop, generated \mathbf{B} in its center consists only of vertical component B_z given by (according to [17]):

$$B_z = \frac{\mu_0 I}{2r}. \quad (5.6)$$

By choosing $I = 20 \text{ A}$ and $r = 5 \text{ cm}$, value $B_{z1} = 1.25664 \text{ T}$ is obtained from equation 5.6. If above-mentioned configuration is calculated by algorithm from equation 5.5, the same value of $B_{z2} = 1.25664 \text{ T}$ is obtained. Since both B_{z1} and B_{z2} are equal, it can be assumed that used algorithm does not introduce any numerical errors into the calculated result.

5.2 Arrangement of B Measurement with Hall Probes

First series of measurements concerning the problem mentioned in the beginning of chapter were made in 2008, when tokamak GOLEM was freshly transferred from Institute of

Plasma Physics to Faculty of Nuclear Sciences and Physical Engineering. In that time, room for its containment was not yet ready, thus tokamak was placed temporarily under large tent in courtyard. This implies its state was very different from the present one, as none of its systems was operational. Since required external poloidal magnetic field was generated by stabilization coils (described in section 4.2.3), they had to be energized by capacitor brought from Institute of Plasma Physics, with its capacity equal to $3.2 F$. The capacitor was charged up to $52.3 V$, with time constant of its discharge being $\tau = 0.5 s$ (time required for magnitude of current in discharge to drop below $1/e$ of initial value). Scheme of used circuit can be found in fig. 5.2. Evolution of current in capacitor discharge was measured by small Rogowski coil encircling conductor connecting energized set of coils with capacitor. Signal of used Rogowski coil was integrated analogically and its calibration constant was equal to $10^{-3} V A^{-1}$. An example of typical evolution of current in this experiment can be found in fig. 5.4 on the left panel.

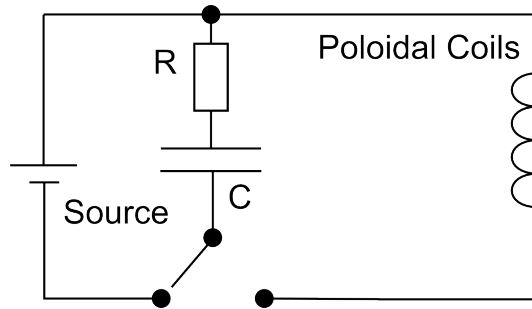


Figure 5.2: Scheme of circuit used for energizing of poloidal coils. C denotes capacitor described in section 5.2.

Sensor	Sensitivity [V/T]
HS1	28.0
HS2	28.0
HS3	27.2
HS4	27.7
HS5	27.5
HS6	26.3

Table 5.1: Calibration constants for Hall probes. The set-up of the probes on the SK ring can be found in fig. 5.3.

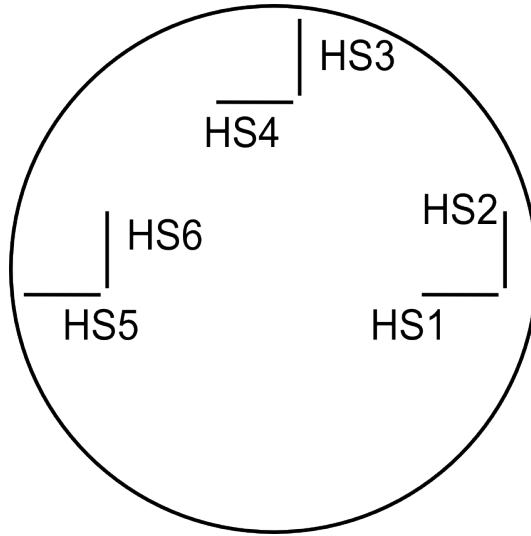


Figure 5.3: Locations of used Hall probes on the diagnostic ring.

Since there are two sets of stabilization coils, one for horizontal field generation and one for vertical field generation (see section 4.2.3), only one set, corresponding to direction of investigated field, was energized at a time. The field itself was measured by ring of Hall probes described in section 4.3.6. Locations on the ring of used Hall probes can be found in fig. 5.3. All the selected probes were calibrated by Helmholtz coils in advance. Please take note that calibration slightly depended on direction of field as well, thus for each probe there were two constants for signal conversion. Resultantly, in analysis of obtained data the direction of measured field had to be taken into consideration as well. Used calibration constants can be found in tab. 5.1. During each discharge, signal of only one hall probe was measured at a time, as one channel of oscilloscope had to be reserved for Rogowski coil.

Used Hall sensors (see fig. 5.3) enabled to measure both vertical and horizontal magnetic field on the top, low-field side and high-field side of the tokamak. Evolution of current was put into algorithm in equation 5.4 resp. 5.5 in order to obtain values of \mathbf{B} . Please take note that since magnetic field was in each case generated by a set of 4 coils, contribution of each of the coils had to be calculated separately. Resultant value was a sum of contributions of all the 4 coils. If the space between the coils and sensor behaved magnetically as vacuum, values obtained from equations 5.4 and 5.5 would be equal to values measured by Hall probes. Comparison between measured values and the calculated ones can be found in section 5.4 on the left panel of figs. 5.5, 5.6, 5.7, 5.8, 5.9, 5.10 and 5.11.

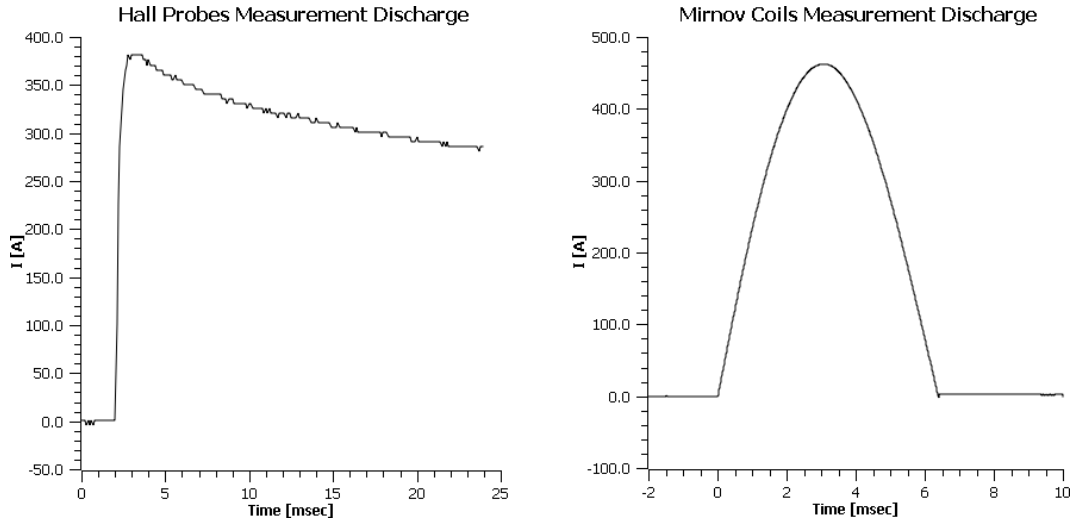


Figure 5.4: An example of current discharges driven through poloidal coils during experimental arrangement with Hall probes (panel on the left) and experimental arrangement with Mirnov coils (panel on the right).

5.3 Arrangement of B Measurement with Mirnov Coils

Measurement from previous section was repeated two years later, in 2010. This time, tokamak was already put in its room and most of its systems were already operational, thus poloidal field coils could be energized by capacitor system located in the cellar below (see fig. 4.1). In this case however, value of time constant τ was much lower than in measurement in section 5.2, even though there was implemented an additional coil into the circuit in an attempt to raise this value. As can be observed in fig. 5.4, lower value of τ resulted in different shape of current discharge evolution. On the other hand, in both the experiments there was generated current of approximately the same magnitude (see fig. 5.4). Evolution of current was, similarly to previous measurement, measured by Rogowski coil, encircling conductor connecting system of energizing capacitors to poloidal field coils. According to [24], calibration constant of this sensor was equal to $6.55 \cdot 10^6 \text{ AV}^{-1}$. Similarly to measurement with Hall probes, a two-channel oscilloscope was used for data-acquisition, signal of Rogowski coil measured by channel 1 and signal of Mirnov coil measured by channel 2. However the *DAS* 1 data-acquisition system (see section 4.1) was used as well, enabling parallel measurement with more Mirnov coils

(DAS 2 was not implemented yet).

Since field generated by poloidal coils was relatively weak, amplitude of measured signal was often below the average value of the noise, which caused unexpected problems with data processing. These problems were often in form of unnatural offsets, observed in most of data after their numerical integration took place. As can be seen in fig. 5.5, magnetic field signal became evident after the signal integration, moreover its amplitude stands high above the level of noise. Therefore there exists possibility that observed problems with noise would not develop, had the signals been integrated by analog means.

As was mentioned in previous paragraphs, external magnetic field was measured by Mirnov coils, described in section 4.3.3 as sensors of poloidal magnetic field. Since there are 4 coils in total, placed on fixed locations and in fixed angles, it is evident from fig. 4.8 and 5.3 that only fields corresponding to Hall probes *HS1*, *HS3* and *HS5* could be measured in this experiment. However, unlike the measurement with Hall probes, horizontal magnetic field at the bottom of the tokamak was measured as well.

Similarly to section 5.2, signals of current, obtained by Rogowski coil, were put into equation 5.4 resp. 5.5. By dividing integrated signal of Mirnov coils by their effective area S_{eff} (to be found in section 4.3.3), values of \mathbf{B} magnitude were obtained. Results of calculations can be found in section 5.4 this time on the right panel of figs. 5.5, 5.6, 5.7, 5.8, 5.9, 5.10 and 5.11.

5.4 Results and Analysis of the Measurements

From obtained results it seems that space between inside of the liner and coils of poloidal stabilization field can be assumed to be of relative permeability equal to 1 only in limited context. As can be seen in figs. 5.5 and 5.6, in the case of vertical field on low-field side and high-field side of the liner, there is a very good agreement between expected and measured values of \mathbf{B} magnitude. On the other hand, evident disagreement between expected values of \mathbf{B} and the measured ones can be observed in the rest of obtained data. In figs. 5.7, 5.8, 5.9, 5.10 and 5.11 there can be seen that measured values of \mathbf{B} magnitude are often twice as high as the expected ones. It is thus assumed that in the cases of vertical field on the top and horizontal field in all the measured locations, behavior of chamber towards outer magnetic field is not equivalent to the one of vacuum, but rather to behavior of material with relative permeability $\mu_r > 1$.

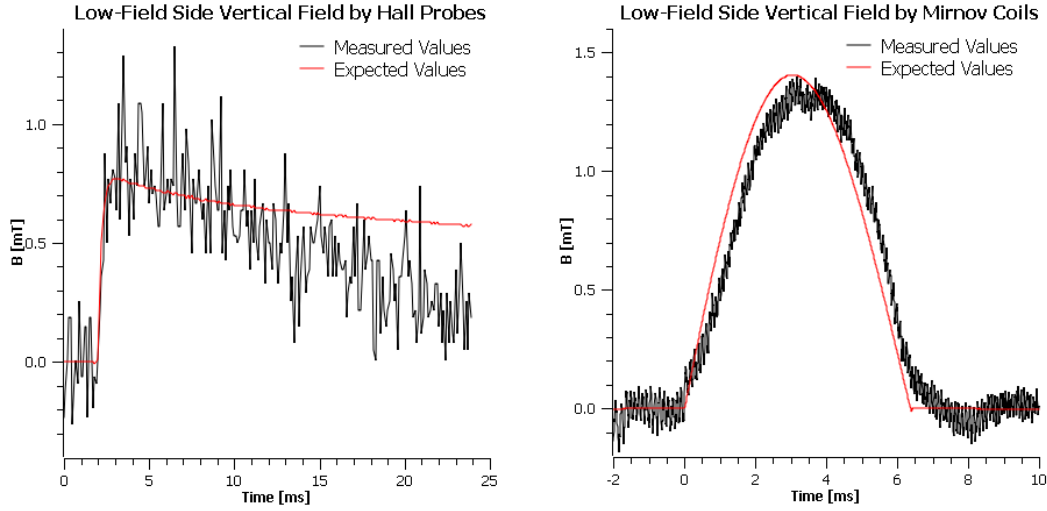


Figure 5.5: Measurement of vertical magnetic field \mathbf{B} on low-field side of liner. Measurement with Hall probe is on the left panel, while measurement with Mirnov coil is on the right panel.

Moreover, results of \mathbf{B} measurement in all the locations show that induced magnetic field increases slower and decreases faster than it should be. By comparison of measured values to the ones calculated from current driven through coils, their difference becomes evident especially on larger time scales (e.g. in measurements with Hall probes). It seems that by induction of magnetic field by poloidal coils, currents in other conducting elements of the tokamak are induced as well. According to Lenz's law, these currents induce magnetic field acting against field of the coils, thus measured values seem to be decreasing more rapidly than they would otherwise. Thus, if larger time scales are considered, material of tokamak between the liner and poloidal coils cannot be assumed to exhibit vacuum-like behavior, regardless on the location in the liner and direction of generated poloidal field.

Additionally, in all the obtained data it can be observed that Hall probes measurements are in very good agreement with Mirnov coils measurements, even though they took place with two-year time difference under very different conditions. This implies that observed phenomena were not caused by cross-talk of signals, nor by errors implemented by sensors, and thus they really characterize properties of tokamak chamber.

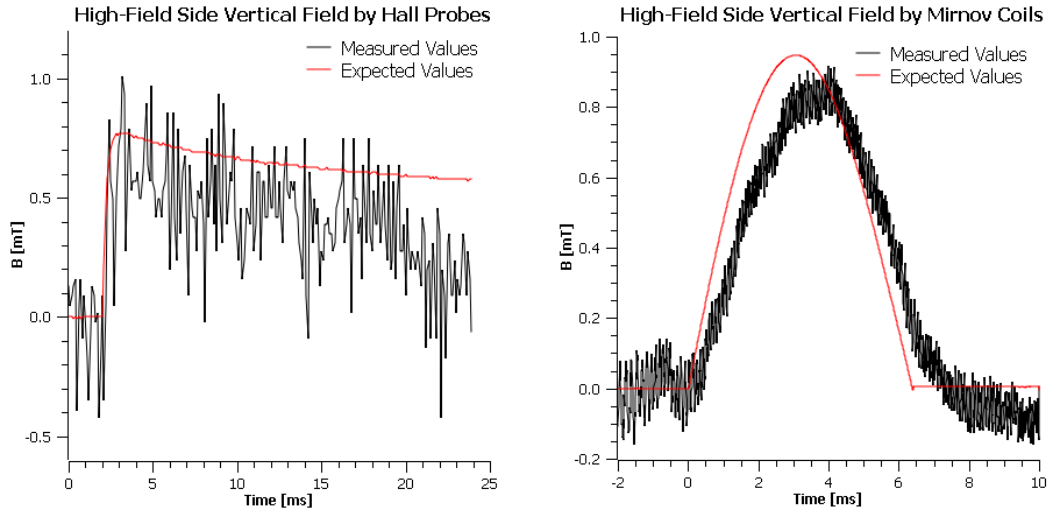


Figure 5.6: Measurement of vertical magnetic field \mathbf{B} on high-field side of liner. Measurement with Hall probe is on the left panel, while measurement with Mirnov coil is on the right panel.

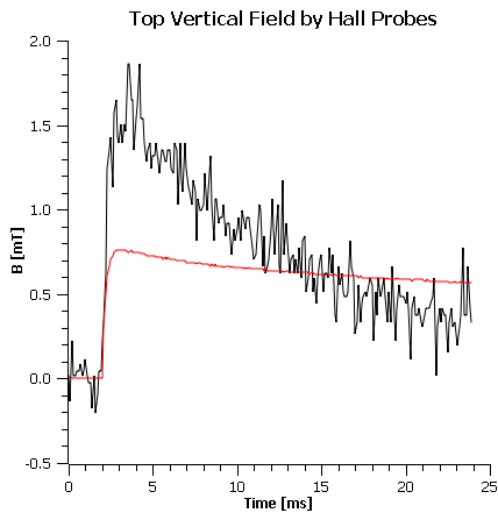


Figure 5.7: Measurement of vertical magnetic field \mathbf{B} on the top of liner, made with a Hall probe.

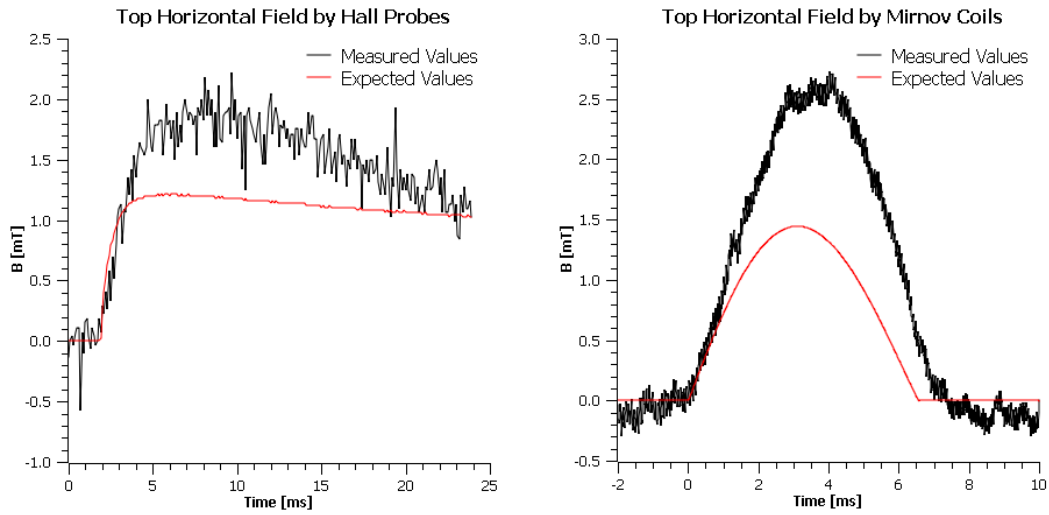


Figure 5.8: Measurement of horizontal magnetic field \mathbf{B} on the top of liner. Measurement with Hall probe is on the left panel, while measurement with Mirnov coil is on the right panel.

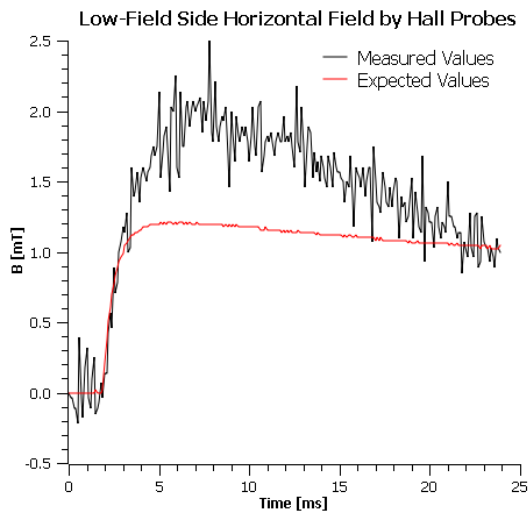


Figure 5.9: Measurement of horizontal magnetic field \mathbf{B} on low-field side of liner, made with a Hall probe.

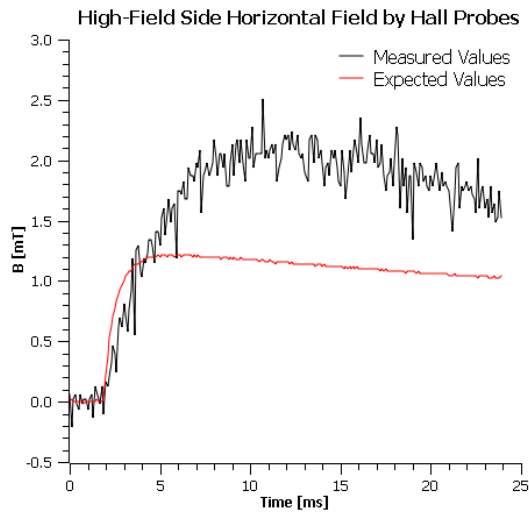


Figure 5.10: Measurement of horizontal magnetic field \mathbf{B} on high-field side of liner, made with a Hall probe.

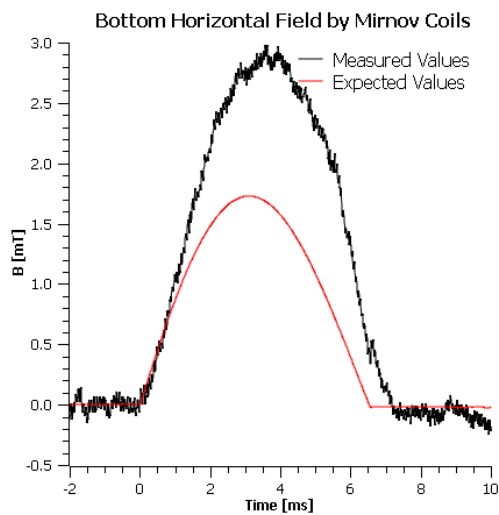


Figure 5.11: Measurement of horizontal magnetic field \mathbf{B} on the bottom of liner, made with a Mirnov coil.

Chapter 6

Plasma Position Estimation

6.1 Theory of Plasma Position Determination and Used Approximation

As was mentioned in section 3.3, magnetic diagnostics can be used for evaluation of plasma column position. Most correct approach to evaluate plasma column displacement is to use Grad-Shafranov equations. According to literature [20], following set of equations was used for these purposes on tokamak CASTOR:

$$\Delta_{HFS} = \frac{B_9 - B_1}{2B_0} b - \frac{1}{2} \left[\ln \frac{b}{a} - 1 + \left(\Lambda - \frac{1}{2} \right) \left(1 + \frac{a^2}{b^2} \right) \right] \frac{b^2}{R}, \quad (6.1)$$

$$\Delta_{BOT} = \frac{B_{13} - B_5}{2B_0} b, \quad (6.2)$$

where

$$\Lambda = \left(\frac{B_9 - B_1}{2} - \bar{B}_z \right) \frac{R}{B_0 b} - \ln \frac{b}{a} + 1, \quad (6.3)$$

and

$$a = a_L - \sqrt{\Delta_{HFS}^2 + \Delta_{BOT}^2}. \quad (6.4)$$

In these equations, Δ_{HFS} (resp. Δ_{BOT}) denotes displacement of plasma column towards high-field side (resp. bottom) of the tokamak and B_i denotes magnetic field measured by respective Mirnov coil (see in fig. 6.1 as well). Value of b is equivalent to distance of Mirnov coils from center of liner (its value is stated in section 4.3.3). R , major radius and a_L limiter radius of tokamak were both stated in section 4.1. Finally, $B_0 = \mu_0 I_p / 2\pi b$, where I_p stands for plasma current. In previous equations, following relations were assumed (and according approximations took place): $|\Lambda - 1|a/R \ll 1$ and $\Delta_i \ll b$. Additionally, literature [20] states that in the case of this tokamak, modulation of poloidal

magnetic field along torus (caused by limbs of transformer and diagnostic windows) is not negligible and thus difference $B_9 - B_1$ needs to be replaced with \bar{B}_{dif} , defined as:

$$\bar{B}_{dif} = (B_9 - B_1) + 2(B_z - \bar{B}_z). \quad (6.5)$$

B_z represents local value of vertical magnetic field (measured by saddle coil from section 4.3.4) and \bar{B}_z is average value of vertical magnetic field (measured by set of flux loops from section 4.3.2). Literature [20] also states that this set of equations can be solved iteratively with first guess given by $a = a_L$.

Please take note that this chapter does not give detailed analysis on position of plasma column, but rather serves as a first approximation of this position. Thus, set of equations 6.1 - 6.4 was simplified so that flux loops and saddle coil would not be needed for estimation of plasma column position, nor values of Λ and a . In other words that diagnostics of Mirnov coils alone would be sufficient. To be more exact, following approximation took place:

Formula for B_0 is equivalent to magnitude of magnetic field of infinitely long linear conductor (according to Ampere's law). If second part of right-hand side of equation 6.1 is omitted (while equation 6.2 is left as it is), and displacement towards low-field side (resp. top) of the tokamak is considered, following set of equations is obtained:

$$\Delta_{LFS} = \frac{B_1 - B_9}{2B_0} b, \quad (6.6)$$

$$\Delta_{TOP} = \frac{B_5 - B_{13}}{2B_0} b. \quad (6.7)$$

Naturally, it was assumed there is no parasitical modulation of poloidal magnetic field (namely that $B_z = \bar{B}_z$) as well. It can be seen, that 6.7 is just another form of original equation 6.2. If plasma position displacement as in fig. 6.1 is assumed, then following expression can be written:

$$B_{1/9} \sim \frac{1}{b \pm \Delta_{LFS}}. \quad (6.8)$$

Similar relation corresponds to displacement towards the top. Hence, equations 6.6 and 6.7 can be modified into forms:

$$\Delta_{LFS} = b \frac{B_1 - B_9}{B_1 + B_9}, \quad (6.9)$$

and

$$\Delta_{TOP} = b \frac{B_5 - B_{13}}{B_5 + B_{13}}, \quad (6.10)$$

where only signals from Mirnov coils are actually needed for estimation of plasma column displacement. This relations can be also found in literature [1], which implies that plasma position was initially determined this way.

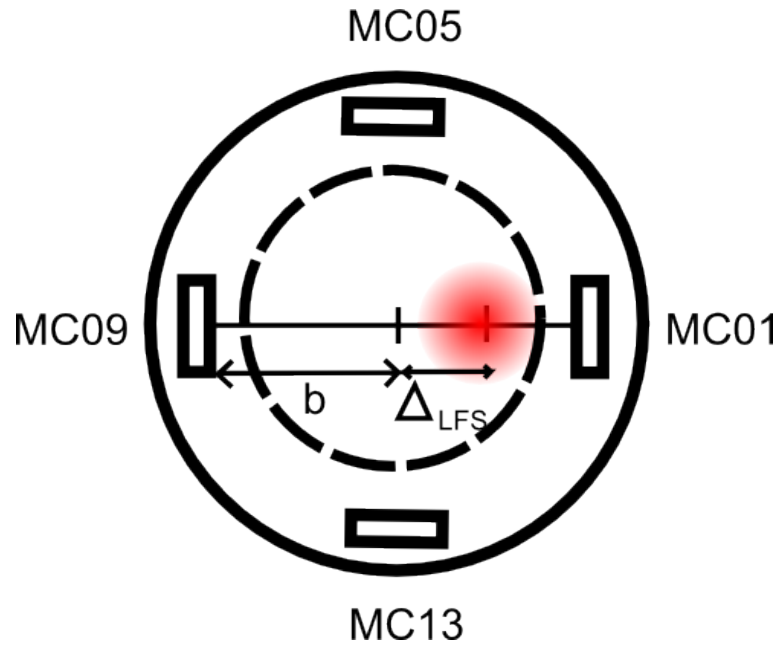


Figure 6.1: Position shift of plasma column (depicted as circle inside of liner) towards low-field side. Dashed circle represents limiter. b denotes distance from center of liner to Mirnov coils and Δ_{LFS} is shift itself. $MC01$ - $MC13$ denote Mirnov coils, where $MC01$ measures magnitude of magnetic field induction B_1 , $MC05$ measures B_5 , $MC09$ measures B_9 and $MC13$ measures B_{13} .

Since this measurement took place some time later than measurement in section 5.3, experimental arrangement corresponds to present status of tokamak, described in chapter 4. Besides Mirnov coils signals, there were measured flux loop voltage, toroidal magnetic field and plasma current as well.

6.2 Subtraction of Toroidal Magnetic Field Cross-Talk

Conditions in this measurement were very different to conditions in measurements described in sections 5.2 and 5.3. Not only there was plasma present inside of liner, but strong toroidal magnetic field as well. Since Mirnov coils are not perfectly aligned, they pick-up a cross-talk signal from toroidal field along with signal of magnetic field generated by plasma. Unfortunately, signal from toroidal field can not be neglected and thus must be subtracted. This subtraction can be done in two possible ways. First is to make a vacuum shot before the actual shot with plasma takes place (given that experimental arrangement will not be changed after the vacuum shot) and then simply subtract raw signal obtained by vacuum shot from raw signal of measurement with plasma.

More general approach, which does not require any vacuum shots to be made in advance, uses data of toroidal magnetic field (measured by small coil described in section 4.3.5). According to Lenz's principle, following equation can be written:

$$\dot{\phi} = S_{tor}\dot{B}_T = U_T, \quad (6.11)$$

where S_{tor} is effective area of coil measuring toroidal field, B_T is toroidal magnetic field and U_T induced voltage on coil. By integrating previous equation and by measuring signal response of this toroidal field on Mirnov coil, following equations for toroidal field coil:

$$B_T = \frac{1}{S_{torr}} \int_0^t U_T d\tau, \quad (6.12)$$

and similarly for Mirnov coil:

$$B_T = \frac{1}{S_{coil}} \int_0^t U_C d\tau, \quad (6.13)$$

are obtained. S_{coil} denotes effective area of coil, whose normal vector is parallel to toroidal field (e.g. represents misalignment of coil) and U_c is voltage signal measured by vacuum shot. By putting previous two equations together it is possible to evaluate constant K_C for conversion of toroidal field signal between coil of toroidal field measurement and Mirnov coil:

$$K_C = \frac{\int U_T d\tau}{\int U_C d\tau}. \quad (6.14)$$

Please take note that each of the Mirnov coils has different K_C constant. If this constant for coil is known, poloidal magnetic field of plasma (subtracted of toroidal magnetic field

influence) can be calculated by following expression:

$$B(t) = \frac{1}{S_{eff}} \int_0^t (U_C(\tau) - \frac{1}{K_C} U_T(\tau)) d\tau. \quad (6.15)$$

In this expression, S_{eff} stands for effective area of Mirnov coil described in section 4.3.3, U_C stands for total voltage on Mirnov coil and U_T is voltage measured on toroidal field measurement coil. Please note that relation 6.15 assumes that data obtained by Mirnov coil are integrated numerically. In the the case of Mirnov coil data being integrated analogically by integrator of time constant RC , by putting equation 3.19 and equation 6.15 together, following expression is obtained:

$$B(t) = \frac{1}{S_{eff}} [RCU_{out}(t) - \frac{1}{K_C} \int_0^t U_T(\tau) d\tau], \quad (6.16)$$

where U_{out} denotes output signal of the integrator.

By making a series of vacuum shots it is possible to obtain statistically sufficient data for evaluation of K_{Ci} constant for every Mirnov coil. These values were calculated by relation 6.14 and can be found in table 6.1. An example of measured magnetic field by Mirnov coil with, and without toroidal magnetic field signal cross-talk can be found in fig. 6.2.

Coil	K_C [-]
MC01	166.736
MC05	76.68
MC09	105.598
MC13	-

Table 6.1: K_C constants for elimination of toroidal magnetic field cross-talk on Mirnov coils (see equation 6.15). Configuration of Mirnov coils is in fig. 6.1. No value in the case of *MC13* means that misalignment of this coil was not detected.

6.3 Results and Analysis

Data in fig. 6.2 represent typical signal on all the Mirnov coils during plasma shot. This figure also serves as a demonstration of results of toroidal magnetic field cross-talk

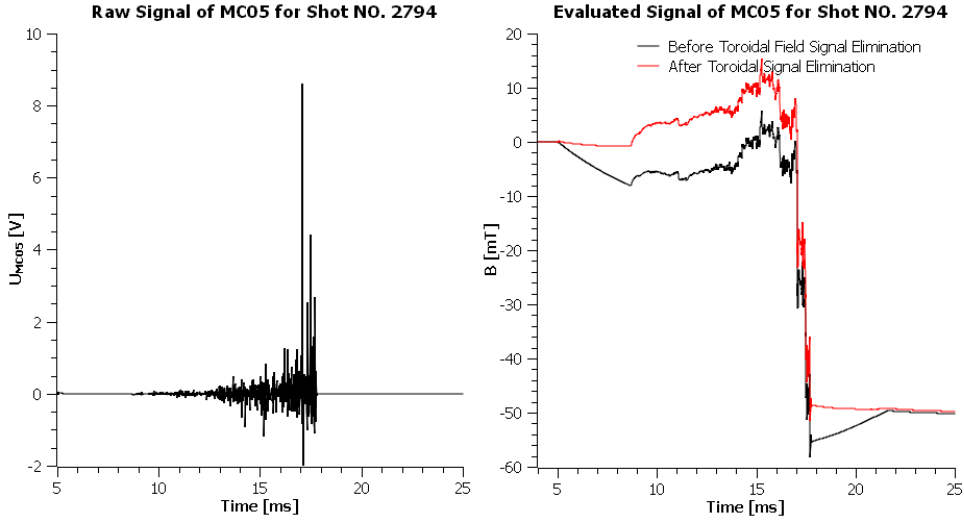


Figure 6.2: An example of Mirnov coil data. The elimination of toroidal magnetic field cross-talk is described in section 6.2.

elimination method described in section 6.2. As can be observed, fluctuations of raw signal are getting stronger with time. From integrated signal it can be seen that data can no longer be relied upon after 16. *ms*. This phenomenon of increasing fluctuations and large values of picked-up signal on the end of discharge can be explained by growth of plasma column instabilities. Since, as was mentioned in section 4.3.3, the frequency bandwidth of Mirnov coils is limited, they cannot follow fast signals of plasma perturbations. Due to that (as can be seen in fig. 6.2), abnormal drops or rises in magnitudes of magnetic field are obtained after integration of signal. As was already proposed in section 4.3.3, this problem could probably be solved by use of passive integrator.

Estimation of plasma column displacement was carried out on two shots - namely shot 2792 and 2794. On left panel in fig. 6.3 and 6.6, an evolution of current is depicted, while flux loop voltage evolution is on the right panel. Time evolution of average toroidal magnetic field (both the sensor and method of calculation are described in section 4.3.5) can be found in fig. 6.4 and 6.7. Finally, displacement of plasma column itself, calculated by equation 6.9 (resp. 6.10), can be found on the left (resp. right) panel in fig. 6.5 and 6.8. Since plasma displacement can take place only inside of the liner (whose radius is $r = 0.1$ *m*), values of displacement greater than this hold no relevant meaning and thus graphs of displacement were scaled to interval of $(-0.1; 0.1)$ *m*.

On both fig. 6.5 and 6.8, one common trait is evident - before generation of plasma column, during large instabilities phase and after the dissipation of plasma column, irrele-

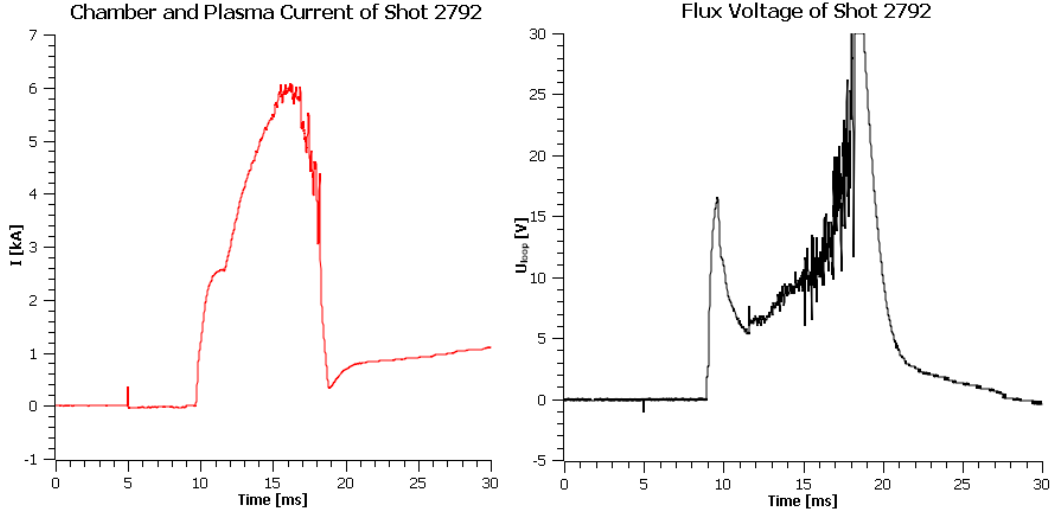


Figure 6.3: Current and flux voltage evolution of shot 2792.

vantly large values of displacement can be observed. This is caused by used equations 6.9 and 6.10, as they have comparative character. However, as soon as plasma is generated, values drop to relevant magnitudes and stay there as long as Mirnov coils are able to react to plasma perturbations.

For shot 2792, moment when values of displacement start to be relevant is located between 9. and 10. *ms* (see fig. 6.5). As can be observed in fig. 6.3, this is also the moment when current starts to flow and sudden decrease in flux voltage is observed (meaning that part of power sent to transformer is transferred to plasma column). Further observations show that until 15. *ms*, plasma column maintains its position in the center of liner, shifted only by 1 *cm* towards both low-field side and bottom. However, in 15. *ms*, a sudden increase in fluctuations is observed (in fig. 6.3 as well). According to fig. 6.5, plasma column seems to have moderately shifted towards high-field side and bottom and moved to top and low-field side of the tokamak afterwards. However (as was shown in fig. 6.2), as soon as intensity of perturbations starts to grow, signals of Mirnov coils can not be longer relied upon. Thus this observed movement of plasma column right before its dissipation does not need to correspond to reality. Again, as was already mentioned, frequency response bandwidth of Mirnov coils could be increased by implementation of analog integrator into data acquisition system.

Evolution of plasma column displacement of shot 2794 holds many similar traits to shot 2792. In fig. 6.8 it can be observed that as plasma is generated between 8. and 9. *ms*, values of displacement start to be relevant. Until 11. *ms*, plasma column maintains its

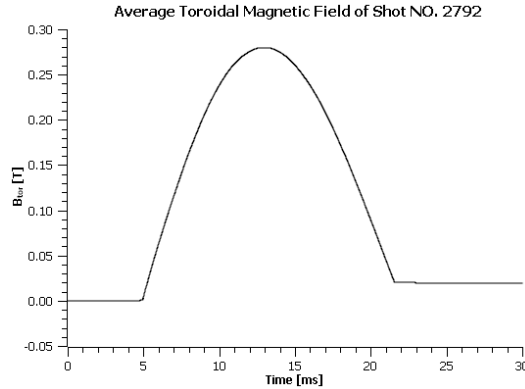


Figure 6.4: Evolution of average toroidal magnetic field during shot 2792, evaluated by method described in section 4.3.5.

horizontal position in the center of liner, while vertically seems to move a little towards top, being generated 1 *cm* towards bottom. Afterwards there is an interesting change of location as plasma column moves about 1.5 *cm* towards low-field side and 1.5 *cm* towards bottom of tokamak. In fig. 6.6 there can be observed, that there are not present any significant fluctuations in that time, rather plasma column seems to be calm. Perturbations can be observed after 13. *ms*, and after 15. *ms* data are once again unreliable, although this time it seems that perturbations had lower frequency and were thus easier for Mirnov coils to follow (see fig. 6.8).

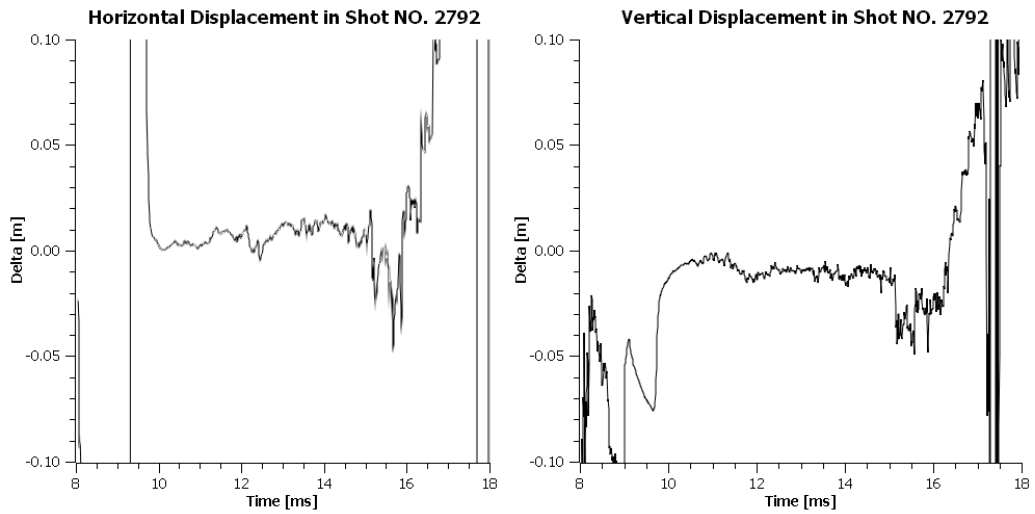


Figure 6.5: Graph on the left panel shows displacement of plasma column towards low-field side, calculated by equation 6.9. Graph on the right panel shows displacement of plasma column towards top, calculated by equation 6.10. Data are relevant for shot 2792.

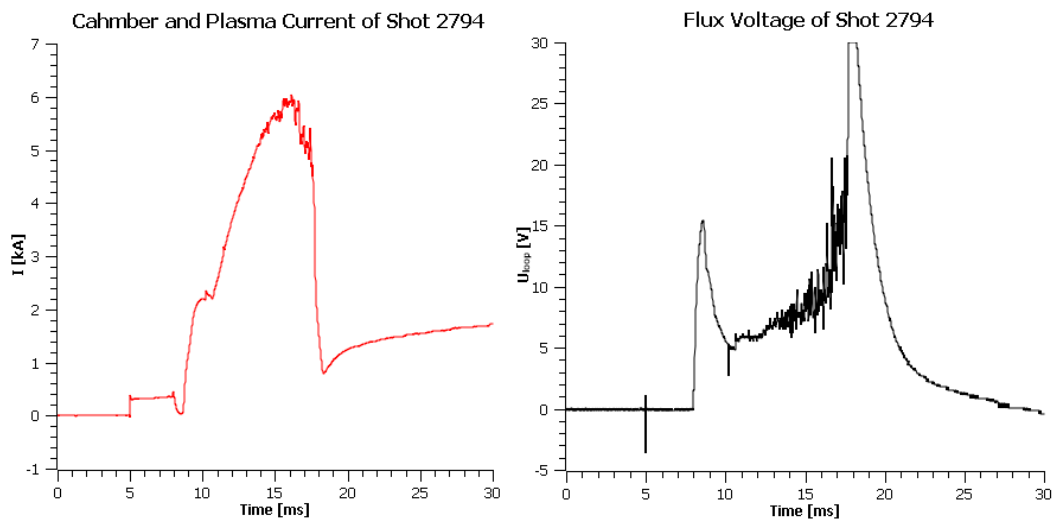


Figure 6.6: Current and flux voltage evolution of shot 2794.

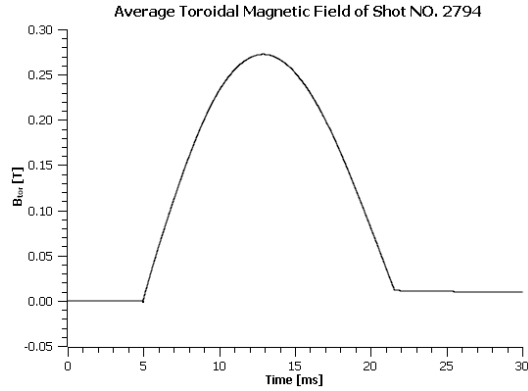


Figure 6.7: Evolution of average toroidal magnetic field during shot 2794, evaluated by method described in section 4.3.5.

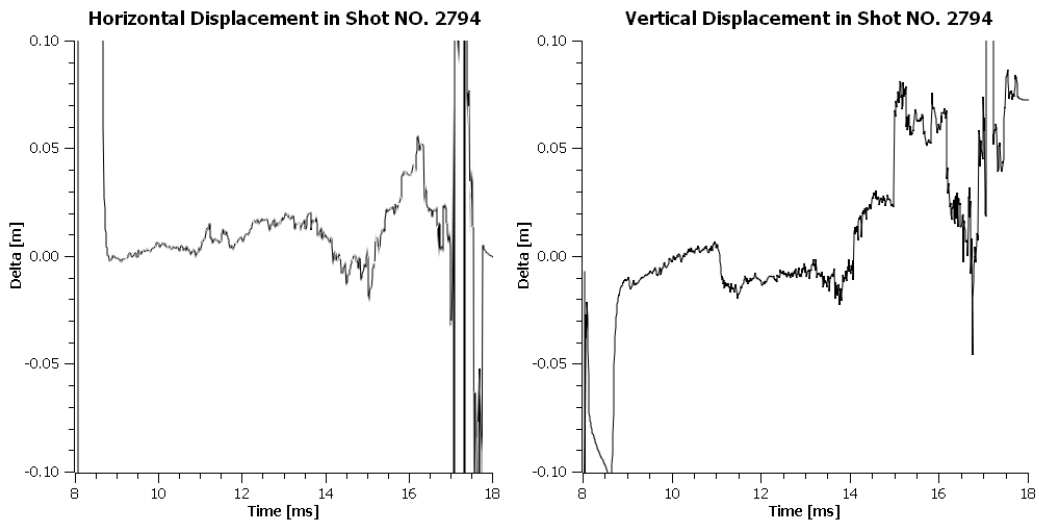


Figure 6.8: Graph on the left panel shows displacement of plasma column towards low-field side, calculated by equation 6.9. Graph on the right panel shows displacement of plasma column towards top, calculated by equation 6.10. Data are relevant for shot 2794.

Chapter 7

Summary

This work provides basic overview of magnetic field configuration in a magnetic confinement concept called tokamak. Additionally, an overview of most common magnetic field sensors is provided as well. After brief introduction into problematic of nuclear fusion, basic properties of tokamak-type device are characterized. The need for presence of poloidal magnetic field, which is induced by current driven through its plasma, is explained by presence of particle drifts. As a strong magnetic field is one of the most critical characterizations of tokamak, basic magnetic diagnostics sensors are described afterwards. Since most of these sensors are of inductive nature, they measure rate of change of magnetic field induction, rather than the quantity itself. This implies that their signal has to be integrated, which can be carried out by numerical or by analog means. A discussion concerning pros and cons of two concepts of analog integration follows. It should be noted that use of analog integration enables to improve bandwidth of frequency response of inductive sensors. On the other hand, magnetic diagnostics with galvanometric sensors, namely Hall probes, have started to be more popular lately, since measured signal is directly proportional to magnetic field and thus does not require integration. Even though radiation damage of these semiconductor sensors might be of issue in potential reactor, sources state that Hall probes still have potential to be part of magnetic diagnostics of ITER, being already implemented in numerous experiments.

The rest of the thesis deals with problematic of present magnetic diagnostics of tokamak GOLEM. After description of present state of this tokamak, especially of systems generating its electric and magnetic fields, a more in-depth description of its magnetic field sensors is provided. Since all the presently used magnetic diagnostics sensors are of inductive nature, their signals have to be integrated, which is presently carried out numerically. This is sufficient for most of the sensors, however it was shown that Mirnov

coils have slow response rate to high frequency signals of plasma perturbations and thus data of these perturbations are useless and cannot be integrated numerically. Therefore, a use of passive integrating circuit is proposed in order to increase frequency response rate of Mirnov coils. Parameters of this circuit were inferred from integrators used on tokamak CASTOR. Although Hall probes are not presently used on tokamak GOLEM, there have been made several experiments with them on this tokamak. In one of these experiments it was shown that there is very good consistency between Hall probes and Mirnov coils measurements, thus Hall probes could replace the Mirnov coils as feedback control sensors.

Furthermore, two different experiments concerning use of magnetic diagnostics have been carried out. In the first experiment, behavior of chamber towards magnetic field induced from outside by coils of poloidal stabilization field was investigated. From the knowledge of evolution of current energizing the coils and their exact spatial configuration, values of expected magnetic field induction magnitude inside of liner were calculated. It was shown that values measured with Hall probes and Mirnov coils were consistent to the calculated ones only in the case of vertical field on high-field side and low-field side of chamber in time scales less than 20 *ms*. The other experiment investigated possibility of plasma position estimation by use of Mirnov coils. Since due to misalignment of Mirnov coils is their signal affected by cross-talk of toroidal magnetic field, a method of elimination of its cross-talk is described. It was shown that plasma column position estimation be used only until massive of plasma perturbations take place, as their frequency is too high for Mirnov coils to follow in their present state.

As tokamak GOLEM is not in its final state of operation yet, more work will have to be done to change this situation, especially in the case of magnetic diagnostics. Many magnetic sensors are still not calibrated and problems with frequency response rate of Mirnov coils have not been solved yet. It would be very interesting to construct and try functionality of proposed integrator circuits on these sensors. Additionally, a new diagnostic ring of Hall probes was said to be in construction and its eventual calibration and implementation into GOLEM diagnostics would undoubtedly be a stimulating challenge. Finally, since magnetic diagnostics is a very wide area of study, further investigations of this area will have to be done. It would be especially interesting to study realization of magnetic diagnostics on other tokamaks as well. Since estimation of plasma column position is investigated, it would be challenging to carry out correct plasma position determination on some other tokamak. Therefore, author will try to focus his following research on matters stated above.

References

- [1] L. Bárdoš, F. Žáček, et al, *Experimentální zařízení tokamak TM-1-MH* [Experimental Device Tokamak TM-1-MH], Ústav fyziky plazmatu Akademie věd České republiky, Institute Report 35/77, December, 1977 (in Czech).
- [2] F.F. Chen, *Introduction to Plasma Physics*, Plenum Press, New York, 1984.
- [3] I. Ďuran, "Fluktuace magnetického pole na tokamaku Castor" [Fluctuations of Magnetic Field on Tokamak CASTOR], doctoral dissertation, Dept. Electronics and Vacuum Physics, Faculty of Mathematics and Physics, Charles Univ. in Prague, 2003 (in Czech).
- [4] I. Ďuran, "Personal Consultation," Prague, 2010.
- [5] I. Ďuran, J. Sentkerestiová, J. Stockel, et al, "Magnetic Measurements Using Array of Integrated Hall Sensors on the CASTOR Tokamak," *Proc. 17th Topical Conference on High-Temperature Plasma Diagnostics*, May, 2008, pp.304-334.
- [6] A.A. Harms, et al, *Principles of Fusion Energy*, World Scientific, 2000.
- [7] "Figure of a Tokamak," <http://www.splung.com/nuclear/images/fusion/tokamak.png> (accessed 23.6.2010).
- [8] J.D. Huba, *NRL Plasma Formulary*, Naval Research Laboratory, 2009.
- [9] I. H. Hutchinson, *Principles of Plasma Diagnostics*, Cambridge University Press, Cambridge, 2002.
- [10] G. Van Oost, et al, "Joint Experiments on Small Tokamaks," 2006.
- [11] R.S. Popovic, *Hall Effect Devices*, IOP Publishing, 2004.

- [12] M. Řípa, *Řízená Termojaderná Syntéza pro každého* [Controlled Thermonuclear Fusion for Everyone], Ústav fyziky plazmatu Akademie věd České republiky, Prague, 2004 (in Czech).
- [13] J. Scheffel and P. Brunzell, *Fusion Physics - Introduction to the Physics Behind Fusion Energy*, Alfvén Laboratory, 2007.
- [14] J. Sentkerestiová, "Systematic Measurements of Plasma Position on CASTOR Tokamak Using Magnetic Coils and Hall Sensors," master's thesis, Dept. Nuclear Reactors, Faculty of Nuclear Sciences and Physical Engineering, Czech Technical Univ. in Prague, 2006.
- [15] J. Stöckel, "Mirnov coils pro měření polohy sloupce plazmatu na tokamaku GOLEM" [Mirnov Coils for Plasma Column Position Measurement on Tokamak GOLEM], E-mail to J. Kocman, 7 April, 2010 (in Czech).
- [16] E.J. Strait, et al, "Magnetic Diagnostics," *Fusion Science and Technology*, vol. 53, February, 2008, pp. 304-334.
- [17] I. Štoll, *Elektrina a Magnetismus* (Electrics and Magnetism), Vydavatelství ČVUT, Prague, 1998 (in Czech).
- [18] V. Svoboda, et al, "Former Tokamak CASTOR Becomes Remotely Controllable GOLEM at the Czech Technical University in Prague," *37th EPS Conference on Plasma Physics*, June, 2010, P2.111.
- [19] S. Tumanski, "Induction Coil Sensors – a Review," *Measurement Science and Technology*, vol. 18, 2007, pp. R31-R46.
- [20] M. Valovič, "Magnetic Diagnostics on the CASTOR Tokamak," *Czechoslovak Journal of Physics*, vol. B 38, 1988, pp. 65-72.
- [21] M. Valovič, "Control of Plasma Position in CASTOR Tokamak," *Czechoslovak Journal of Physics*, vol. B 39, 1989, pp. 1111-1119.
- [22] J.A. Wesson, *Tokamaks*, Clarendon Press, Oxford, 2004.
- [23] F. Žáček, "Re: kalibracni konstanty civek" [Re: Calibration Constants of the Coils], E-mail to V. Svoboda, 1 March, 2010 (in Czech).
- [24] F. Žáček, E-mail to V. Svoboda, March, 2010 (in Czech).